REPORT DOCUMENTATION PAGE

AFOSR-TR-97

0263

1. AGENCY USE ONLY (Leave blank)	2. REPORT DATE	3. REPORT TYPE AND DATES COVERED
	October 31, 1996	Final Report 5/1/94- 8/31/96

4. TITLE AND SUBTITLE	5. FUNDING NUMBERS
Modeling of InP Crystal Growth by the MLEK Process	AFOSR Contract F48620-94-C-0035

6. AUTHOR(S)

Steven A. Orszag, Vadim Borue, Ananias Tomboulides, Eytan Barouch

7. PERFORMING ORGANIZATION NAME(S) AND ADDRESS(ES)	8. PERFORMING ORGANIZATION REPORT NUMBER
Cambridge Hydrodynamics, Inc. P.O. Box 1403 Princeton, NJ 08542	

9. SPONSORING/MONITORING AGENCY NAME(S) AND ADDRESS(ES)	10. SPONSORING/MONITORING AGENCY REPORT NUMBER
Air Force Office of Scientific Research Bolling AFB Washington, DC 20332	

11. SUPPLEMENTARY NOTES

12a. DISTRIBUTION/AVAILABILITY STATEMENT

Unclassified/unlimited

DISTRIBUTION STATEMENT A
Approved for public release
Distribution Unlimited

12b. DISTRIBUTION CODE

13. ABSTRACT (Maximum 200 words)

The goal of this work is to achieve prototype simulations of the MLEK process for growth of InP crystals. We have made several key advances in this work, including numerical simulations of three-dimensional time-dependent low Prandtl-number melt convection, with differential rotation, and magnetic fields. To do this we have developed a 3D general-geometry spectral element code. We have demonstrated how rotation and, especially, differential rotation can stabilize melt flows and how magnetic fields can also stabilize these flows. We have also shown that magnetic fields, in certain parameter regimes, can act, somewhat surprisingly, to destabilize the flow. We have also extended our renormalization-group-based turbulence models to describe stratified flows across the full range of low-moderate-high stratification.

DTIC QUALITY INSPECTED 3

14. SUBJECT TERMS	15. NUMBER OF PAGES
	46
	16. PRICE CODE

17. SECURITY CLASSIFICATION OF REPORT	18. SECURITY CLASSIFICATION OF THIS PAGE	19. SECURITY CLASSIFICATION OF ABSTRACT	20. LIMITATION OF ABSTRACT
Unclassified	Unclassified	Unclassified	Unclassified

Modeling of InP Crystal Growth by the MLEK Process

Steven A. Orszag, Vadim Borue, Ananias Tomboulidas & Eytan Barouch

Cambridge Hydrodynamics, Inc. P.O. Box 1403, Princeton, NJ 08542

Abstract

The goal of this work is to achieve prototype simulations of the MLEK process for growth of InP crystals. We have made several key advances in this work, including numerical simulations of three-dimensional time-dependent low Prandtl-number melt convection, with differential rotation, and magnetic fields. To do this we have developed a 3D general-geometry spectral element code. We have demonstrated how rotation and, especially, differential rotation can stabilize melt flows and how magnetic fields can also stabilize these flows. We have also shown that magnetic fields, in certain parameter regimes, can act, somewhat surprisingly, to destabilize the flow. We have also extended our renormalization-group-based turbulence models to describe stratified flows across the full range of low-moderate-high stratification.

1

1 Introduction

Indium Phosphide (InP) offers much promise for advanced photoelectronic and electronic device development because of its attractive physical properties that allow high power, high frequency, and short gate lengths. However, the growth of InP crystals involves a number of major technological challenges because of the need to use high-pressure environments (due to the high vapor pressure of the melt), the difficulty of working with the volatile component phosphorus, the complex stoichiometry of the mixtures involved, and the sensitivity of the grown crystals to defects, twinning, and other imperfections. An attractive method to grow InP crystals in practice is the use of the magnetic liquid encapsulated Kyropoulos (MLEK) technique but the complexity of this process limits the opportunity to use trial-and-error experimental techniques to optimize the crystal growing process.

In our work under AFOSR Contract F49620-94-C-0035, we have made much progress in the simulation of the flow fields involved in the MLEK and related growth processes. We have made several key advances in this work, including numerical simulations at low Prandtl number melt convection with rotation, differential rotation, and magnetic fields. We have demonstrated how rotation and, especially, differential rotation can stabilize melt flows and how magnetic fields can also stabilize these flows. We have also shown that magnetic fields, in certain parameter regimes, can act, somewhat surprisingly, to destabilize the flow. We have developed a simplified model that illustrates this effect of magnetic fields. We have also extended our renormalization-group-based turbulence model to describe stratified flows across the full range of low-moderate-high stratification. Our simulations give the first, spectrally accurate, simulations of 3D low Prandtl number convection with coupled rotation, differential rotation, and magnetic field. As such, we believe that they represent a change in the state-of-the-art of crystal growth modeling and simulation. In addition, our turbulence transport model for stratification should find wide application to problems of Air Force interest. For example, the new model can enable advances in the problem of the dynamics of aircraft wake vortices in stratified atmospheres, a problem with applications to both civilian and military aircraft (e.g., if stratification can cause trailing vortices to bounce off a stratified atmospheric layer into the path of trailing aircraft).

2   Technical Background - Simulation of Melt Flows

We have studied flows in crystal melts in several situations. First, we consider a model problem consisting of a cylindrical crucible of radius R and height H (see Figure 1). Here we have a prototype crystal with radius r, such that $r/R = 0.5$, being pulled from the top surface of the melt. The crystal is allowed to rotate at an angular velocity Ω_2 different from the one of the crucible Ω_1. The solid vertical and bottom boundaries of the crucible are maintained at constant non-dimensional temperature of $T_1 = 2$, whereas the crystal-melt interface is at a fixed temperature of $T_2 = 1$. The top free surface is assumed to have negligible heat flux to the surrounding gas (an assumption which is sometimes removed). The equations of motion are the incompressible Navier-Stokes equations, together with the Boussinesq approximation for the effect of the heating. The length used for non-dimensionalization is the radius of the crucible R, whereas the non-dimensionalizing temperature is the difference $T_1 - T_2$.

The boundary condition at the top is modified in order to include radiation or other kinds of heat-loss, whereas the base of the crucible can be insulated instead of being at constant temperature. The process of crystal growth could potentially be represented by a suction velocity v_c at the crystal-melt interface, but this velocity is usually negligible when compared to the motion of the fluid.

Assuming that we always work in the frame of reference of the rotating crucible, and that the Boussinesq approximation is valid, the equations of motion are

$$\frac{\partial \mathbf{v}}{\partial t} + \mathbf{v} \cdot \nabla \mathbf{v} = -\nabla p - 2\Omega_1 \times \mathbf{v} + \frac{\beta g (T_1 - T_2) R}{U^2} T + \frac{\nu}{UR} \nabla^2 \mathbf{v}$$

$$\frac{\partial T}{\partial t} + \mathbf{v} \cdot \nabla T = \frac{\alpha}{UR} \nabla^2 T$$

(1)

Depending on the choice of the reference velocity scale U, the relevant non-dimensional parameters can be quite different.

For a problem without rotation of any sort, governed purely by *natural convection*, and assuming that the geometry is fixed and the aspect ratios H/D (where $D = 2R$) and r/R

3

MLEK method

B_0

W_2

Crystal

$T_2 = 0$

Free Surface
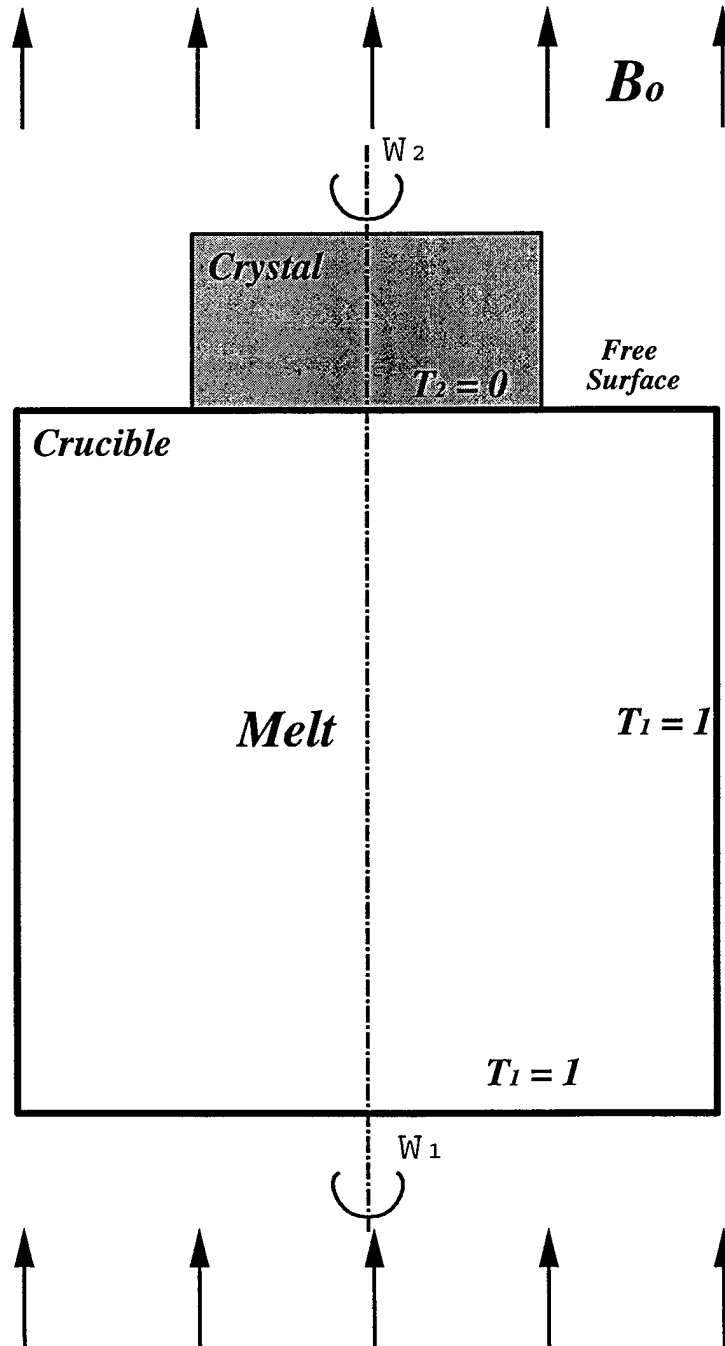
Crucible

Melt

$T_1 = 1$

$T_1 = 1$

W_1

Figure 1: Geometric configuration of crystal melt crucible

are constant, the relevant parameters are the Grasshof number, and the Prandtl number, defined as:

$$Gr = \frac{\beta g (T_1 - T_2) R^3}{\nu^2} \tag{2}$$

$$Pr = \frac{\nu}{\alpha} \tag{3}$$

and the corresponding non-dimensionalized equations become:

$$\frac{\partial \mathbf{v}}{\partial t} + \mathbf{v} \cdot \nabla \mathbf{v} = -\nabla p + T + \frac{1}{Re} \nabla^2 \mathbf{v}$$

$$\frac{\partial T}{\partial t} + \mathbf{v} \cdot \nabla T = \frac{1}{RePr} \nabla^2 T \tag{4}$$

when U is chosen to be $U = \nu/RGr^{1/2}$. Here $Re = Gr^{1/2}$. These are the actual forms of the equations that we use for the case of pure natural convection.

In the case of *rotation*, the non-dimensionalization can be based on either a diffusive velocity scale (as in the non-rotating case), or a scale which is defined by rotation, i.e. $U = \Omega R$. In this case, there is one more non-dimensional parameter in addition to Gr and Pr, the Ekman number E, defined as:

$$E = \frac{\nu}{R^2 \Omega_1} \tag{5}$$

Assuming that U is still $U = \nu/RGr^{1/2}$, the corresponding non-dimensionalized equations become:

$$\frac{\partial \mathbf{v}}{\partial t} + \mathbf{v} \cdot \nabla \mathbf{v} = -\nabla p - 2 \frac{\hat{k} \times \mathbf{v}}{ReE} + T + \frac{1}{Re} \nabla^2 \mathbf{v}$$

$$\frac{\partial T}{\partial t} + \mathbf{v} \cdot \nabla T = \frac{1}{RePr} \nabla^2 T \tag{6}$$

5

where $\hat{k}$ is the direction of rotation Ω_1 (here aligned with the z axis), and Re is again equal to $Re = Gr^{1/2}$.

Finally, when there is also differential rotation between the crucible Ω_1 and the crystal Ω_2, the Rossby number is also important:

$$Ro = \frac{2(\Omega_1 - \Omega_2)}{(\Omega_1 + \Omega_2)} \tag{7}$$

and its influence comes only through the boundary conditions at the crystal-melt interface.

Following Jones [2] the range of parameters may be subdivided into the following five regimes.

Regime I: Heating.

No rotation is assumed. The relevant problem is convection in a vertically heated slot. The flow is typically three-dimensional and unsteady, because of natural convection, for most practical ranges of Gr number. In addition, at the free surface, "spoke" instability patterns could be formed due to heat loss to surrounding environment.

Regime II: Crucible rotation.

In pure form ($Gr = 0$) the relevant problems are stability of the flow around a rotating disk (Ekman layer) and the stability of the flow inside the rotating crucible, [3], [4].

Regime III: Differential rotation.

This regime includes instabilities connected with regime II, but also includes new instabilities due to the dynamics of the shear layer between the rotating crystal and the crucible melt. An interesting problem to study is at which Rossby number the flow becomes non axisymmetric.

Regime IV: Disk rotation with heating.

This is a regime where geostrophic motion can be expected. Usually rotation somewhat suppresses instabilities, even though unsteady three-dimensional flow, because of baroclinic instabilities, can be expected. An interesting problem to study is what is the optimal rotation

frequency that maximally suppresses thermal convection instabilities.

Regime V: Differential rotation with heating.

This regime is similar to regime IV, but the motion can be non axisymmetric because of both baroclinic instabilities, and because of shear layer instabilities arising from the differential rotation.

3   Numerical Results: Simulation of Melt Flows

The numerical experiments that we have performed are both two-dimensional and three-dimensional and extend all the way from Regime I with only natural convection, to Regime V which includes heating and differential rotation. Here we confine ourselves to some representative results, with detailed results presented in papers now in the publication process, [1]. The code used for all these studies is a general geometry spectral element code with high order accuracy in space and time. Numerous resolution studies (discussed in the papers mentioned above) have been performed to ensure the accuracy and reliability of the results presented here.

3.1   Crystal melt flow - 2D simulations

3.1.1   High aspect ratio crucible H/D=1

The values of the parameters used in these simulations were chosen so that they correspond to the values used by [5] in the simulation of buoyancy driven convection in Si melts. The particular case picked was one in the unsteady regime, as reported in [5], and corresponds to a value of $Gr = 2.8 \times 10^6$, with $Pr = 0.03$. The simulations reported in that paper are three-dimensional however. The aspect ratio of the crucible for this set of simulations is $H/D = 1$.

The flow starts from rest and Gr is gradually increased from $10,000$ to $40,000$ and then to 2.8×10^6. The first two simulations reach a steady state and then the flow and temperature

field at $Gr = 40,000$ is used as an initial condition for the calculation at $Gr = 2.8 \times 10^6$. Time history of several flow variables for this run is plotted in Figure (2). It can clearly be seen that even for this axisymmetric case, the flow is unsteady with moderate amplitude fluctuations. Taking into account that the axisymmetric mode is usually very stable, and that it is typically the first or second azimuthal mode that goes unstable first, this result can be interpreted as an instability of the three-dimensional flow as well.

After the pure boyancy driven flow reaches a quasi steady state, rotation is introduced in order to study its effect on the stabilization of the flow. The magnitude of rotation introduced gives a value of the Ekman number $E = Gr^{-1/2} \approx 1.67 \times 10^{-3}$, which is typical of rotation frequencies in practice. The effect of rotation on the flow is quite significant, since it immediately reduces the amplitude of the fluctuations as seen in Figure (2), for times $t > 87.5$. The fact that the flow is becoming stabilized with rotation in the axisymmetric regime, does not necessarily mean that it is also stable if the flow is allowed to be three-dimensional. Therefore three-dimensional simulations were performed. The three dimensional simulations were initiated by using the two dimensional field with rotation at $t = 172.5$ as an initial condition.

The difference between the flow structure with and without rotation is illustrated in Figures (4), and (5), respectively. As can be observed in the Figures, the flow with no rotation consists of the recirculating cells, and the cold fluid is able to convect all the way to the bottom of the crucible; on the other hand, in the case of rotation, there exists only one recirculation cell and the amplitude of the fluctuations is much smaller. The difference between the amplitude of the vorticity field generated by the thermal convection for the two cases is demonstrated in Figure (6) where the maximum vorticity in the bulk of the flow is of order $\mathcal{O}(10)$ without rotation and $\mathcal{O}(1)$ with rotation. For both cases the global maxima of vorticity occur on the side walls of the crucible, as expected for such high Grasshof numbers.

3.1.2 Low aspect ratio crucible H/D=0.25

Several simulations were carried out for a crucible with an aspect ratio of $H/D = 0.25$, since low aspect ratio crucibles are more common in practice. The runs performed for this
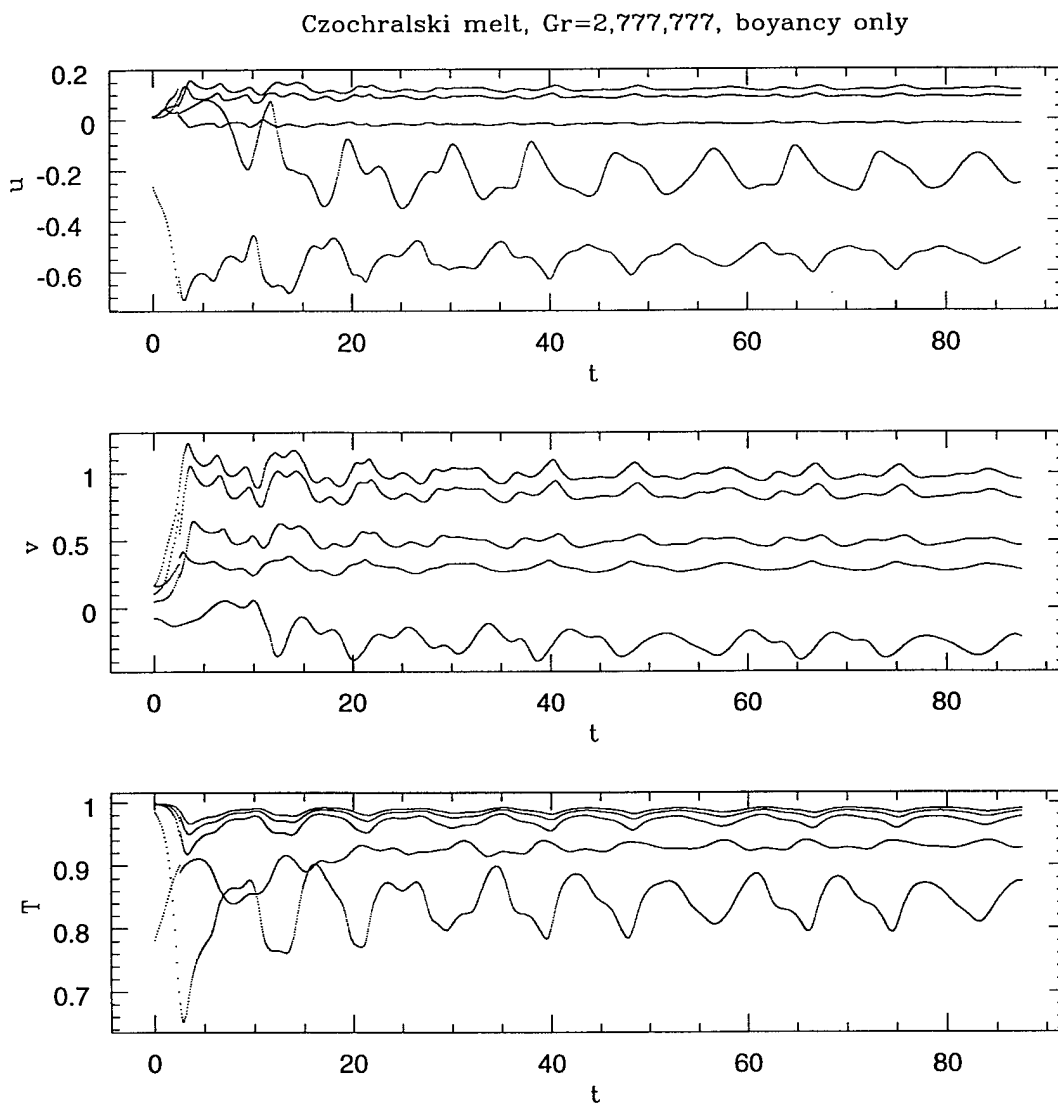
Czochralski melt, Gr=2,777,777, boyancy only

Figure 2: Time history of u,v,T for $Gr = 2.8 \times 10^6$, pure boyancy, axisymmetric

9

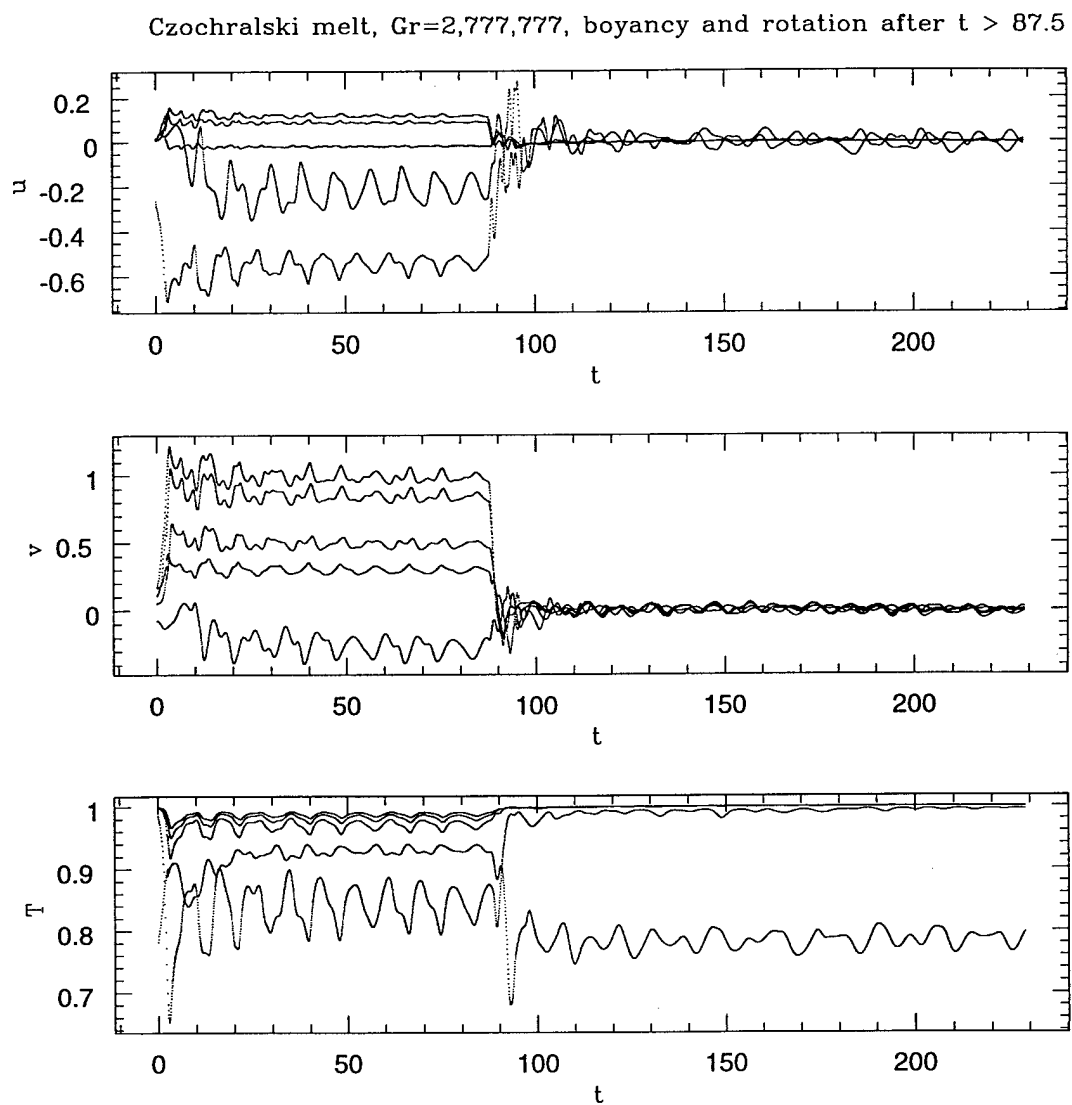Czochralski melt, Gr=2,777,777, boyancy and rotation after t > 87.5

Figure 3: Time history of u,v,T for $Gr = 2.8 \times 10^6$, boyancy and rotation for $t > 87.5$, axisymmetric
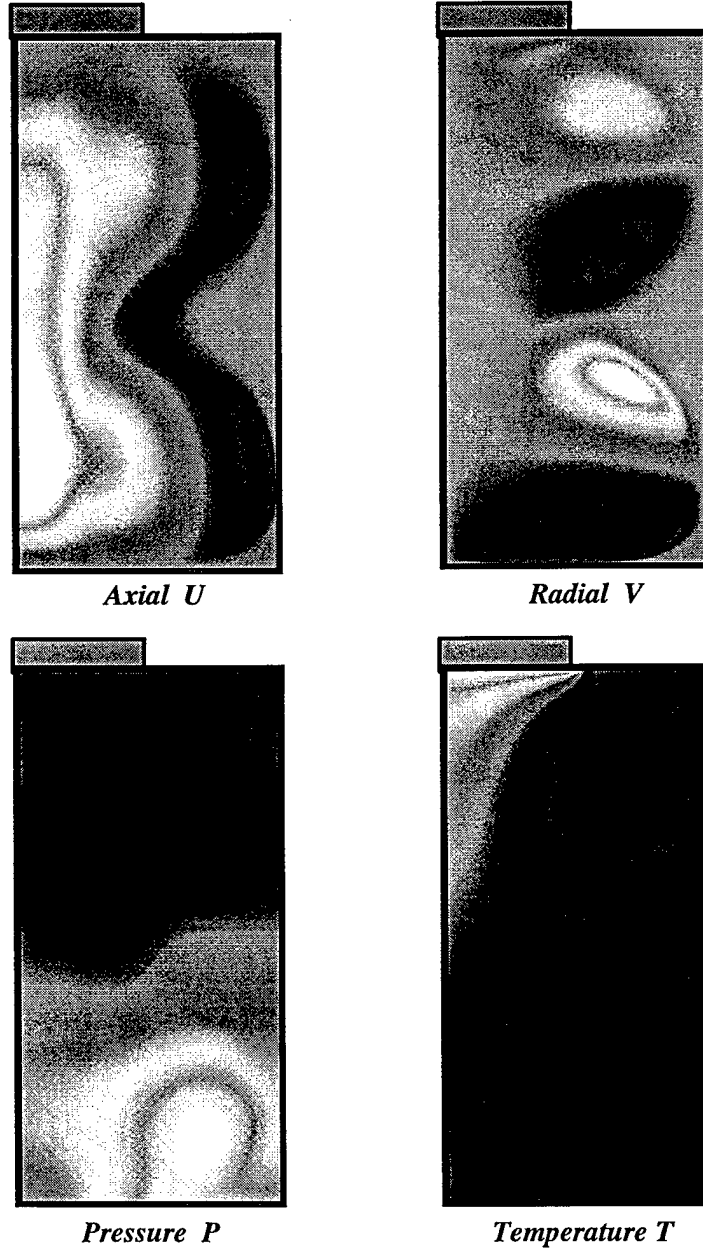
No Rotation
$Gr=2.8x10^6$, Axisymmetric

Axial U

Radial V

Pressure P

Temperature T

Figure 4: Instantaneous flow field without rotation for crucible with H/D=1, axisymmetric

Rotation
$Gr=2.8x10^6$, $E=6x10^{-4}$ Axisymmetric

Axial U   Radial V   Azimuthal W

Pressure P   Temperature T
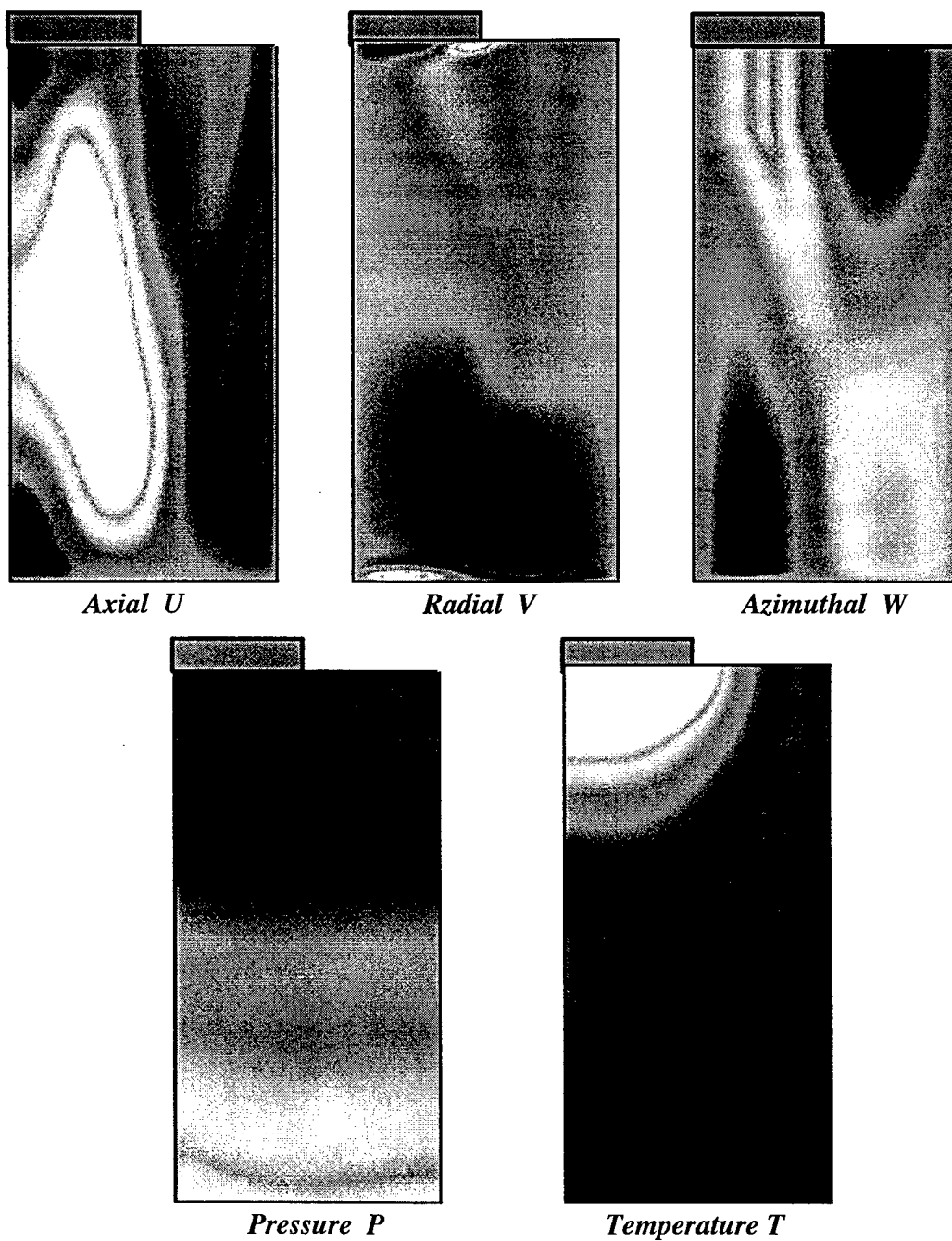
Figure 5: Instantaneous flow field with rotation for crucible with H/D=1, axisymmetric

Axisymmetric–Vorticity

$$Gr=2.8x10^{6}$$

$$Gr=2.8x10^{6}$$
$$E= 6x10^{-4}$$
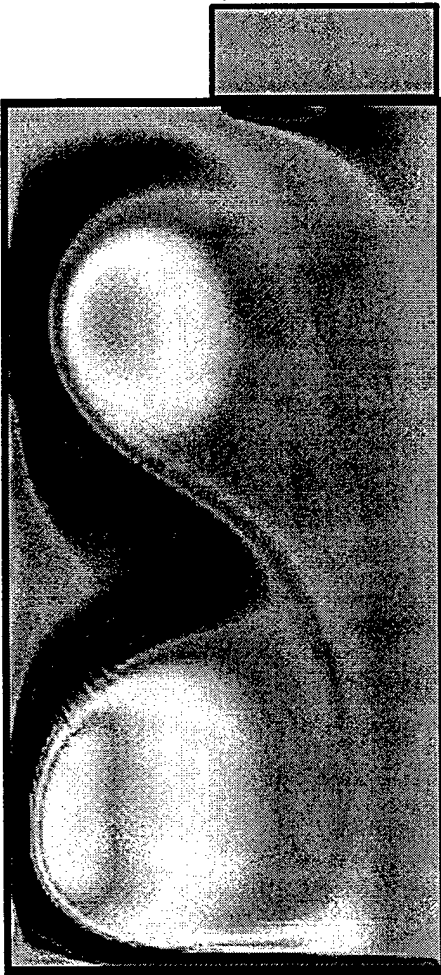
scale: [–7, +7]

scale: [–0.5, +0.5]

Figure 6: Instantaneous vorticity field (a) without rotation and (b) with rotation, for crucible with H/D=1, axisymmetric

configuration again range from 2-D simulations to 3-D simulations with rotation and natural convection; the effect of crystal differential rotation has not been investigated yet. The value of the Grasshof number used in the simulations was picked in a way such that a comparison between the high ($H/D = 1$) and the low ($H/D = 0.25$) aspect ratio crucibles is meaningful. Keeping all other parameters the same, the length scale used for non-dimensionalization can be either $L = (HR)^{1/2}$ or $L = (HR^2)^{1/3}$, which results in an equivalent Gr number, for the low aspect ratio crucible, equal to 2.8×10^6 or 4.4×10^6 respectively. This value is equal or higher than the one used for the high aspect ratio crucible and one might expect a more chaotic flow to be present. In addition, one has to take into account the fact that now the total volume of the liquid metal is double the one corresponding to the high aspect ratio crucible, for the same diameter crystal grown.

The 2-D simulations at the Gr number mentioned in the previous paragraph, reached a steady state for the low aspect ratio crucible. Since the 2-D flow for the high aspect ratio crucible $H/D = 1$ is time dependent with an order 1 amplitude of velocity fluctuations, this fact already implies that flow in the low aspect ratio crucible is less unstable and will possibly lead to smaller fluctuations in the 3-D flow as well. Moreover, isocontours of azimuthal vorticity indicate the presence of only one vortical cell structure in the crucible, whereas two such structures are present in the axisymmetric simulations for the high aspect ratio crucible. This can be observed in Figure (8) where isocontours of flow variables from the steady state field are plotted. As can be observed in the figure, there exists a small pocket of stagnant fluid close to the lower right hand corner of the crucible, which could be a potential source of instability; this implies that a rounded crucible, following the streamlines could be more effective in stabilizing the flow. Time histories of flow components at several points inside the crucible are plotted in figure (7), and as can be observed all values reach a steady state for long times.

3.1.3 Rounded low aspect ratio crucible H/D=0.25

Besides a low aspect ratio, the crucibles used in practice are rounded at the bottom so that they have no abrupt corners. Therefore, our current and near future studies are focusing on crucible shapes similar to the one shown in figure (9) which is a combination of a cylindrical

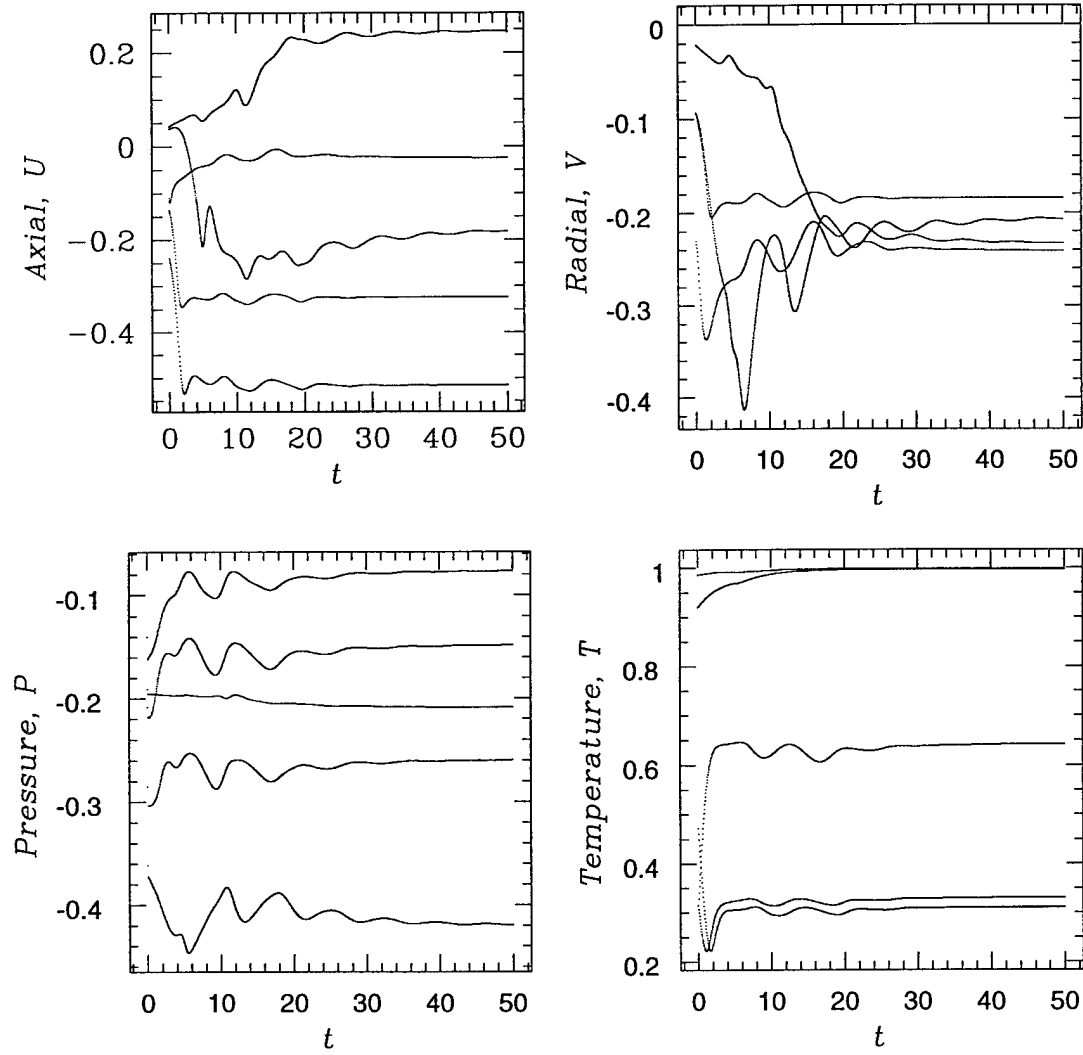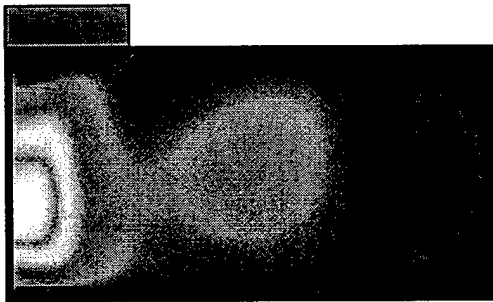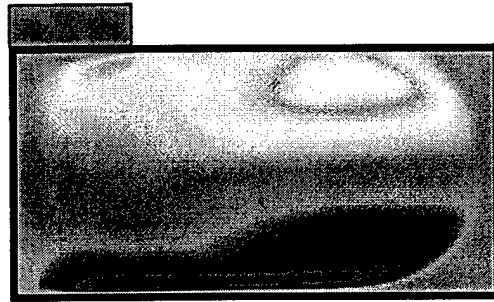Low aspect ratio crucible, Gr=2.8x10⁶, Axisymmetric

Figure 7: Time history of velocity, pressure and temperature for axisymmetric flow in low aspect ratio crucible at $Gr = 2.8 \times 10^6$
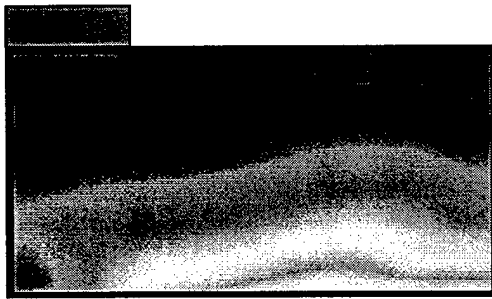
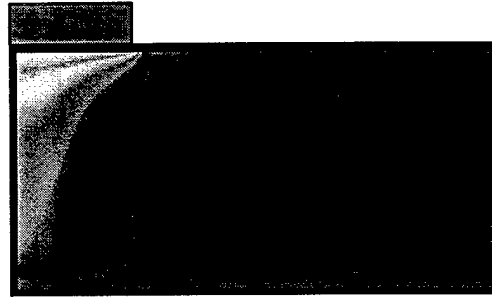# Low Aspect Ratio Crucible:
Axisymmetric Steady state
Gr=2.8x10^6

Axial U: −0.72, 0.41

Radial V: −0.43, 0.73

Pressure P: −1.02, 0.05

Temperature T: 0, 1

Figure 8: Steady state flow field for crucible with aspect ratio H/D=0.25, and $Gr = 2.8 \times 10^6$

part on top and an ellipsoid part at the bottom. The simulations performed up to now are only axisymmetric and as can be observed in figure (10), the flow at $Gr = 2.8 \times 10^6$ reaches a steady state, in a way similar to the flow in the low aspect ratio crucible with corners. As can be observed in Figure (9), the flow again consists of only one recirculating cell, but now the crucible rounded wall follows closely the flow streamline structure.

3.2   Crystal melt flow - 3D simulations

These simulations start with initial conditions from the 2D simulations at $Gr = 2.8 \times 10^6$ by imposing a perturbation on the first azimuthal mode of total energy of the order of 10^{-7}. Two different types of simulations are illustrated here, with high aspect ratio crucible $H/D = 1$, and with low aspect ratio $H/D = 0.25$.

3.2.1   High aspect ratio crucible H/D=1

1. Heating, Crucible Rotation, Differential Crystal Rotation

An example is simulation with rotation of both the crucible and differential rotation of the crystal with Rossby number $Ro = 2$. These simulations show that the flow gradually develops three-dimensionality in the $m = 2$ azimuthal mode, possibly due to shear layer instabilities because of the differential rotation, whereas the $m = 1$ perturbation decays in time, implying that baroclinic instability might not be present. In general, the transition to three-dimensionality, is a much slower one (than the natural convection case), and it involves only even azimuthal modes (m=2,4,6,..). The time history of the energy of the first three even azimuthal modes is shown with a solid line in Figure (11); the first three odd modes are plotted as solid lines in Figure (15). A typical azimuthal energy spectrum is shown in Figure (16) where the difference between the amplitudes of the even versus odd modes is evident.

Isocontours of instantaneous flow variables on both $r - z$ and $r - \phi$ planes are shown in Figures (12), and (13), respectively, and as can be observed - especially from temperature isocontours - the flow demonstrates an even $m = 2$ symmetry.
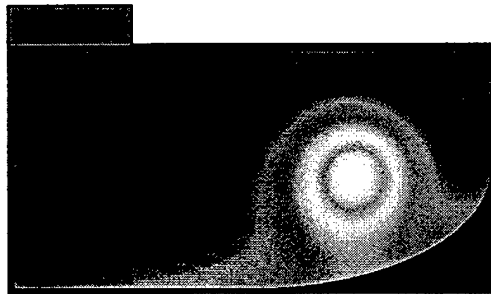
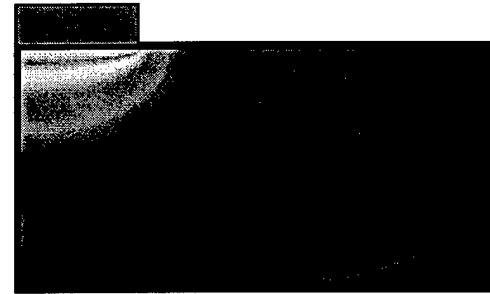# Rounded Crucible:
Axisymmetric Steady state
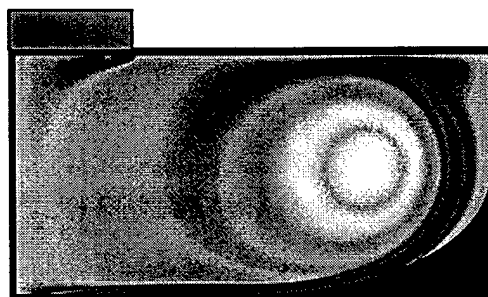### Gr=2.8x10^6
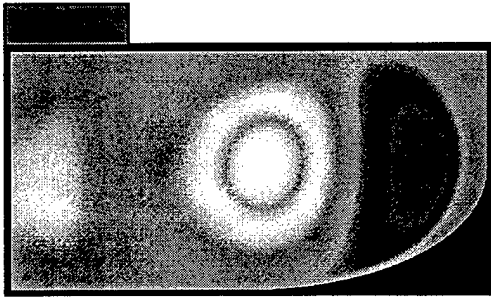
Axial U: −0.78, 0.96

Radial V: −1.01, 1.02

Pressure P: −1.42, 0.065

Temperature T: 0, 1

Vorticity: −8.6, 63.5

Figure 9: Isocontours of velocity, pressure, temperature, and vorticity shown for rounded crucible with heating at $Gr = 2.8 \times 10^6$.

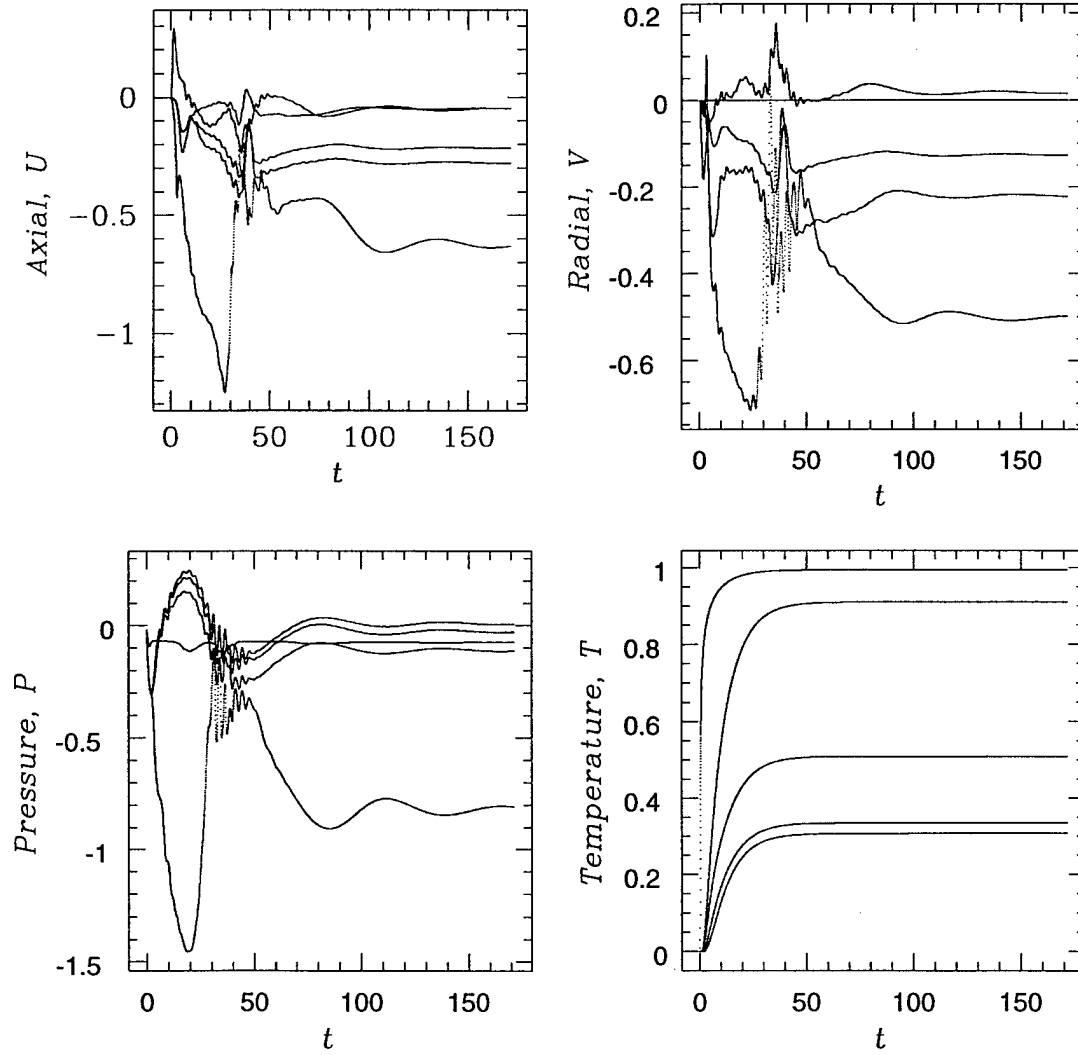Rounded crucible, Gr=2.8x10⁶, Axisymmetric

Figure 10: Time history of velocity, pressure and temperature for axisymmetric flow in rounded crucible at $Gr = 2.8 \times 10^6$

The structure of the flow in terms of axial vorticity isocontours is shown in Figure (14); as can be observed from the figure, there is clearly a symmetry in the flow associated with the $m = 2$ mode, which is dominant, demonstrating itself as one main cyclonic vortex and two counter-rotating ones. This picture is similar to experimental observations reported in [8], where the experiment involved isothermal rotation of a disk inside a rotating crucible.

2. Heating

Simulations with pure natural convection. At $t = 80.0$, and after the three-dimensional flow discussed above developed some three-dimensionality showing that only even modes are growing, rotation was stopped in order to see what the corresponding final states of the flow would be without rotation. The results are shown as dotted lines which start at $t = 80.0$, in Figures (11) and (15). As soon as rotation is stopped, all non-axisymmetric modes increase sharply in energy. This might be an indication that for the range of parameters used in practice, pure natural convection can be violently three-dimensional and unsteady, whereas rotation stabilizes the flow and reduces the fluctuation levels. In some cases it might even be that rotation prevents three-dimensionality. As can be observed in Figures (17), and (18), which show isocontours of flow variables on $r - z$ and $r - \phi$ planes, the flow is quite chaotic and no particular symmetries are evident. Also, although the Prandtl number is very low, low temperature fluid from the top of the crucible convects all the way to the bottom of the crucible, indicative of the large amplitude fluctuations present in the flow.

3. Heating, Crucible Rotation

The results of simulations with natural convection and only crucible rotation show that as soon as differential rotation of the crystal is stopped, at $t = 232.5$, the three-dimensionality rapidly increases, since now all non-axisymmetric modes (even and odd) grow in time. This can again be observed in Figures (11)-(15) by noting the dotted lines which start at $t = 232.5$ and increase in amplitude. The amplitude of observed fluctuations in this case seems to be much larger than for the case of differential rotation, but it still seems to be smaller than for the pure natural convection case. In addition, the flow structure for the case with rotation (but no differential rotation), shown in Figures (19) and (20), is not as chaotic as the pure natural convection case, described in the previous paragraph, although there is still no
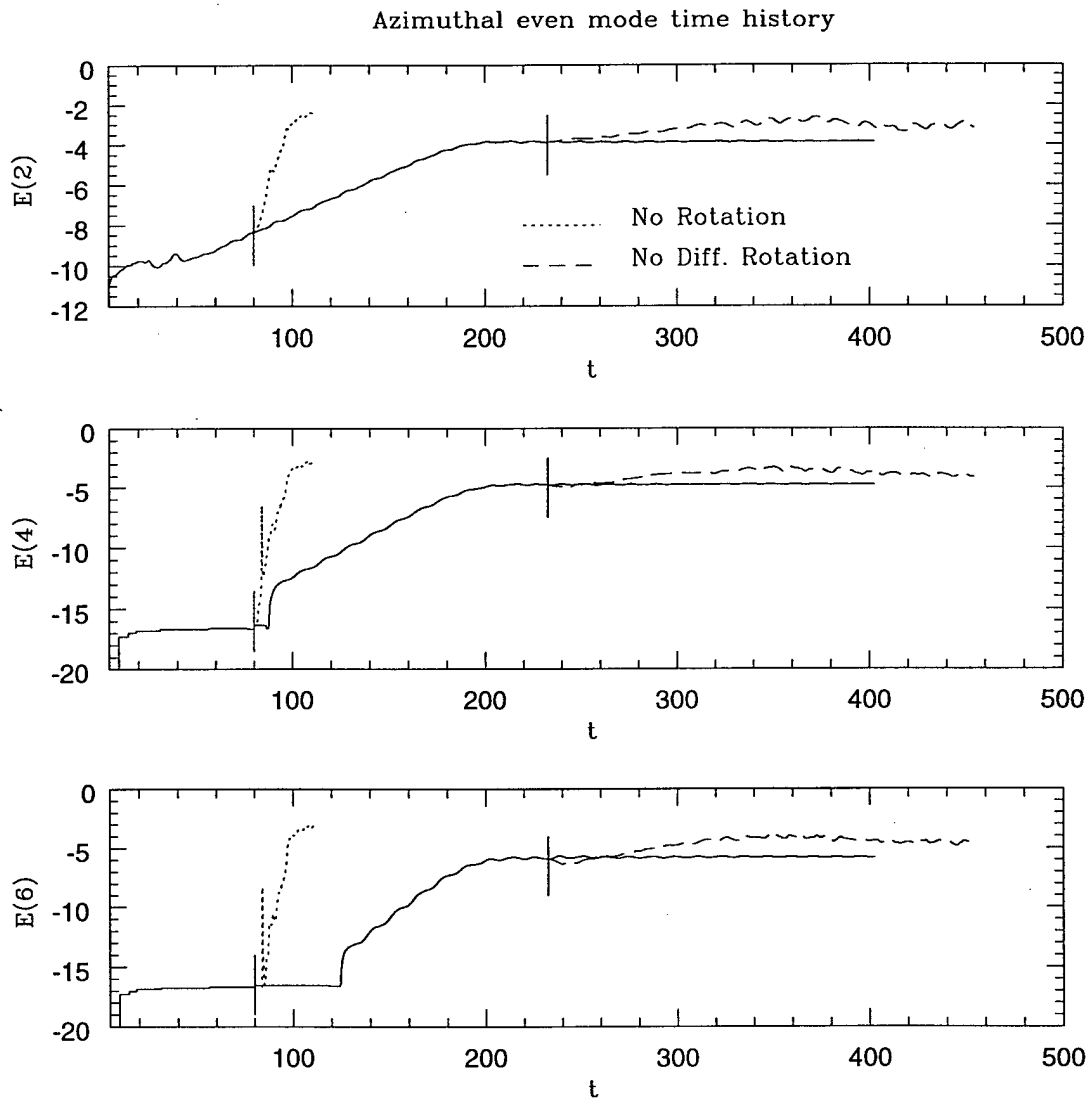
Azimuthal even mode time history

Figure 11: Time history of even azimuthal mode energies

Rotation–Diff. Rotation
$Gr=2.8x10^6$, $E=6x10^{-4}$, $Ro=1$

Axial U

Radial V

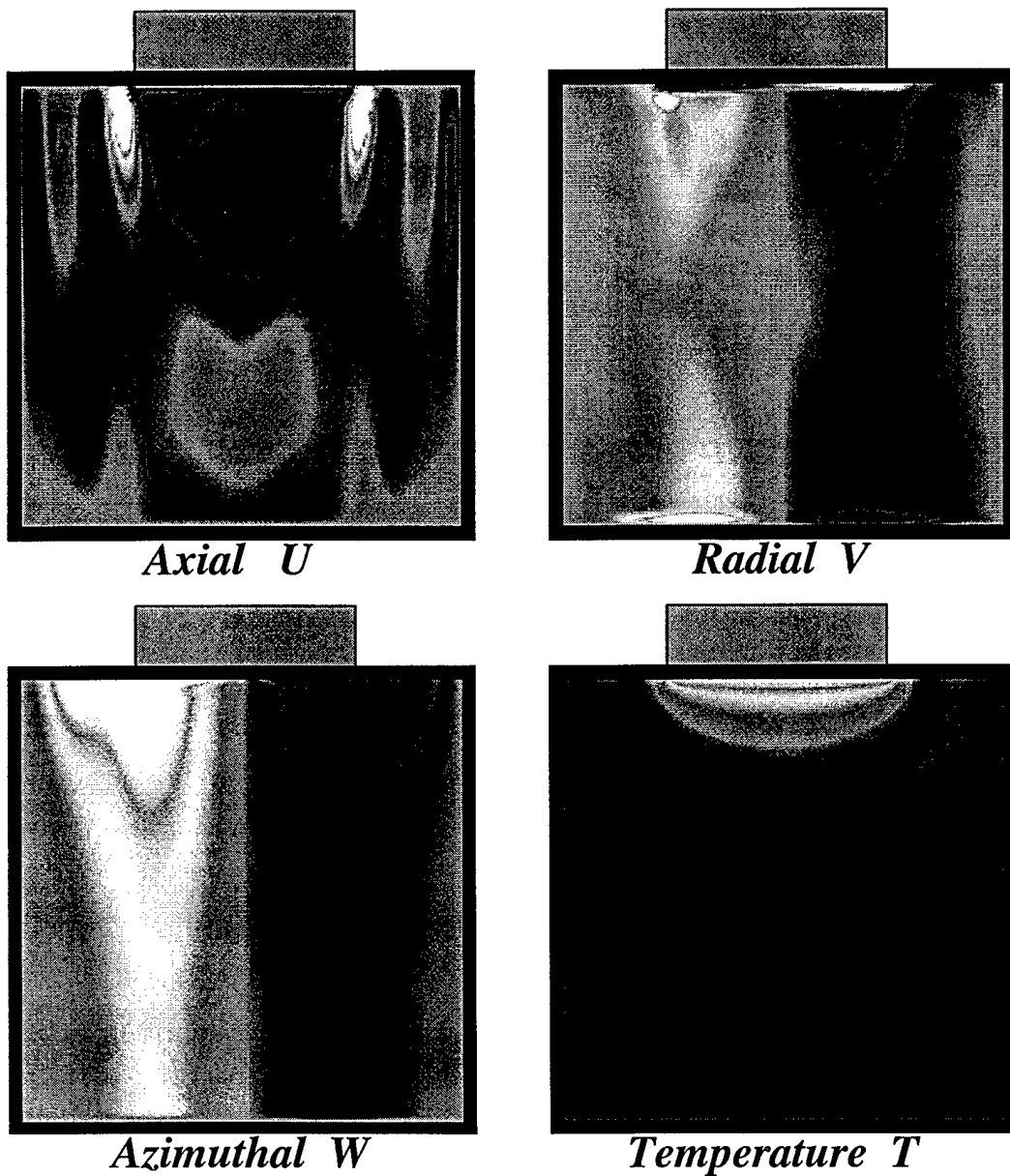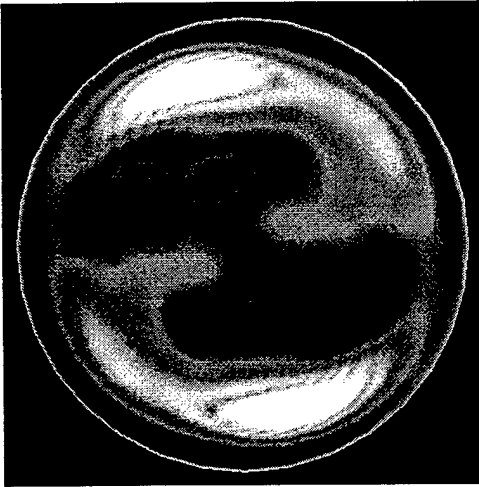Azimuthal W

Temperature T

Figure 12: Instantaneous isocontours of flow variables on a $r-z$ plane for case with heating rotation, and differential rotation
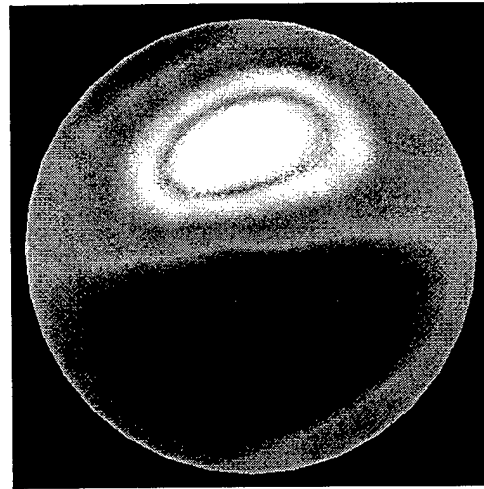
22

Rotation–Diff. Rotation

$Gr=2.8x10^6$, $E=6x10^{-4}$, $Ro=1$

z=1

z=1

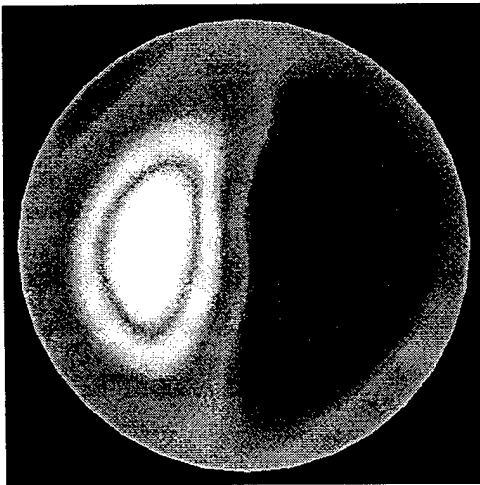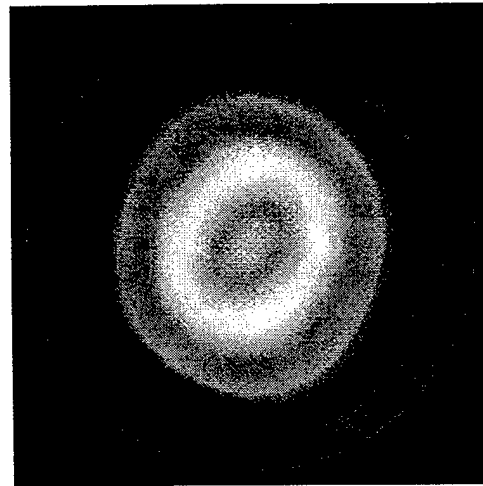Axial U

Radial V

z=1

z=1.75

Azimuthal W

Temperature T

Figure 13: Instantaneous isocontours of flow variables on a $r - \phi$ plane for case with heating rotation, and differential rotation
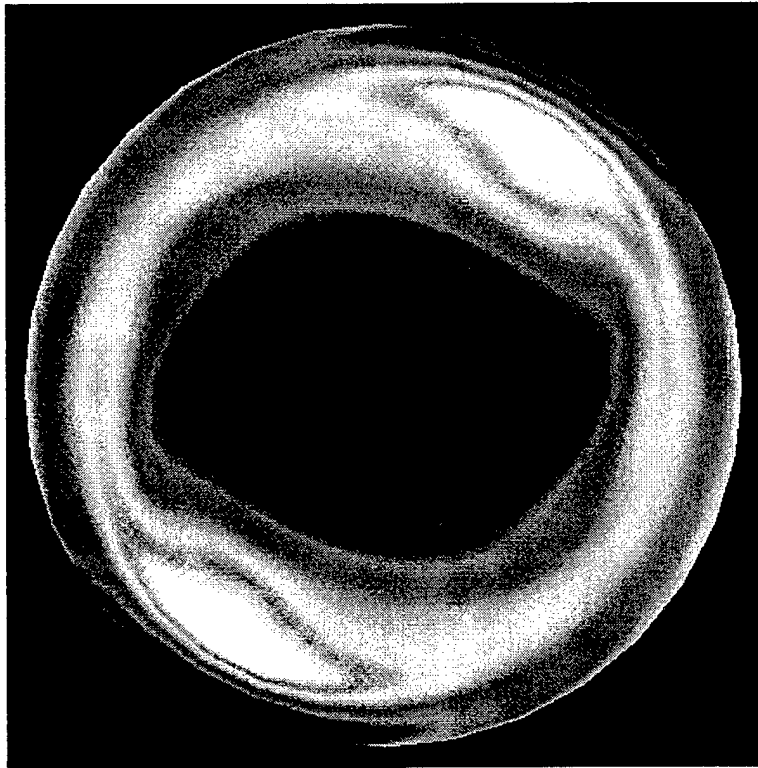
Figure 14: Isocontours of axial vorticity at $z = 1$ for case with heating rotation, and differential rotation
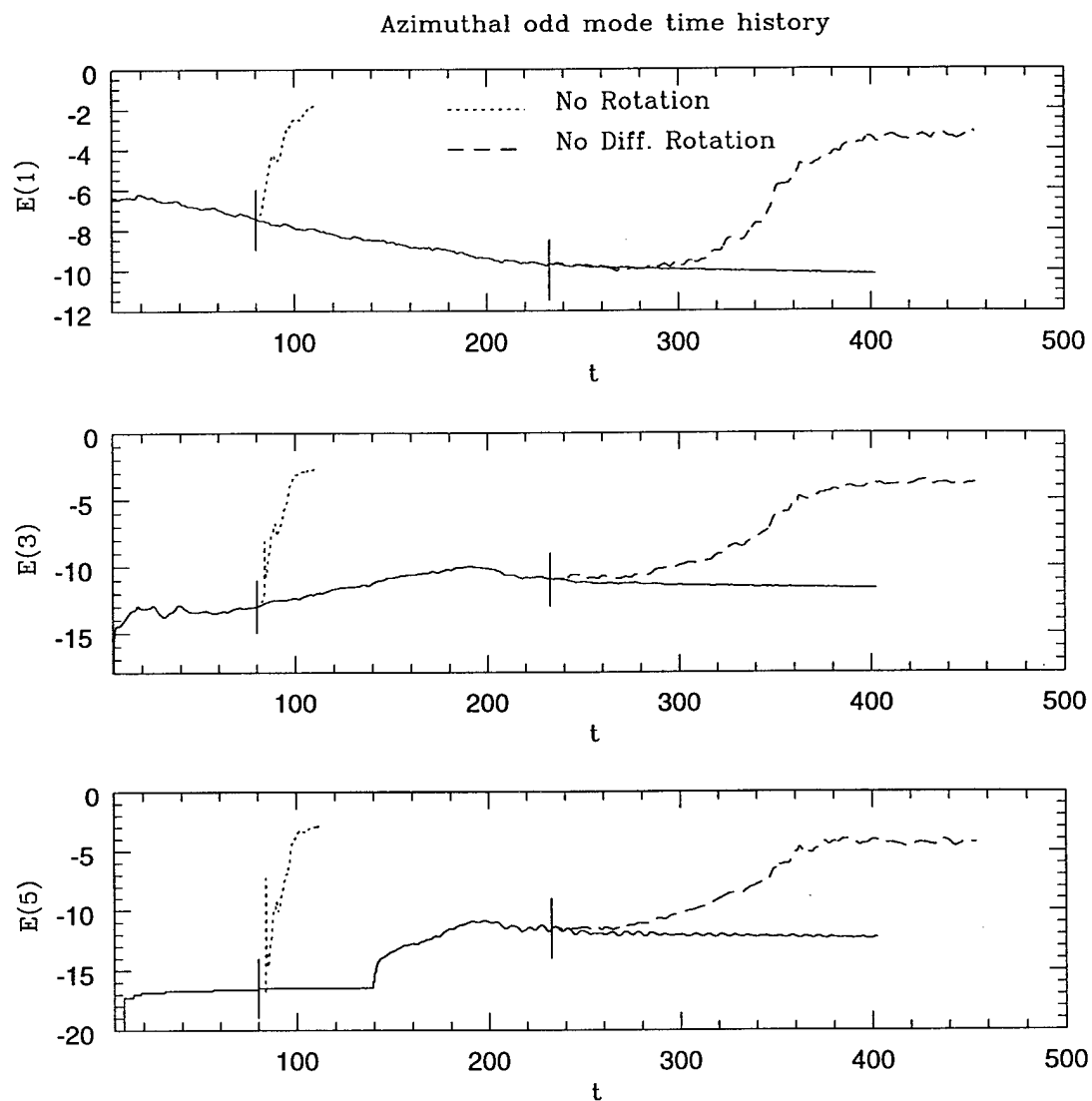
Azimuthal odd mode time history

Figure 15: Time history of odd azimuthal mode energies
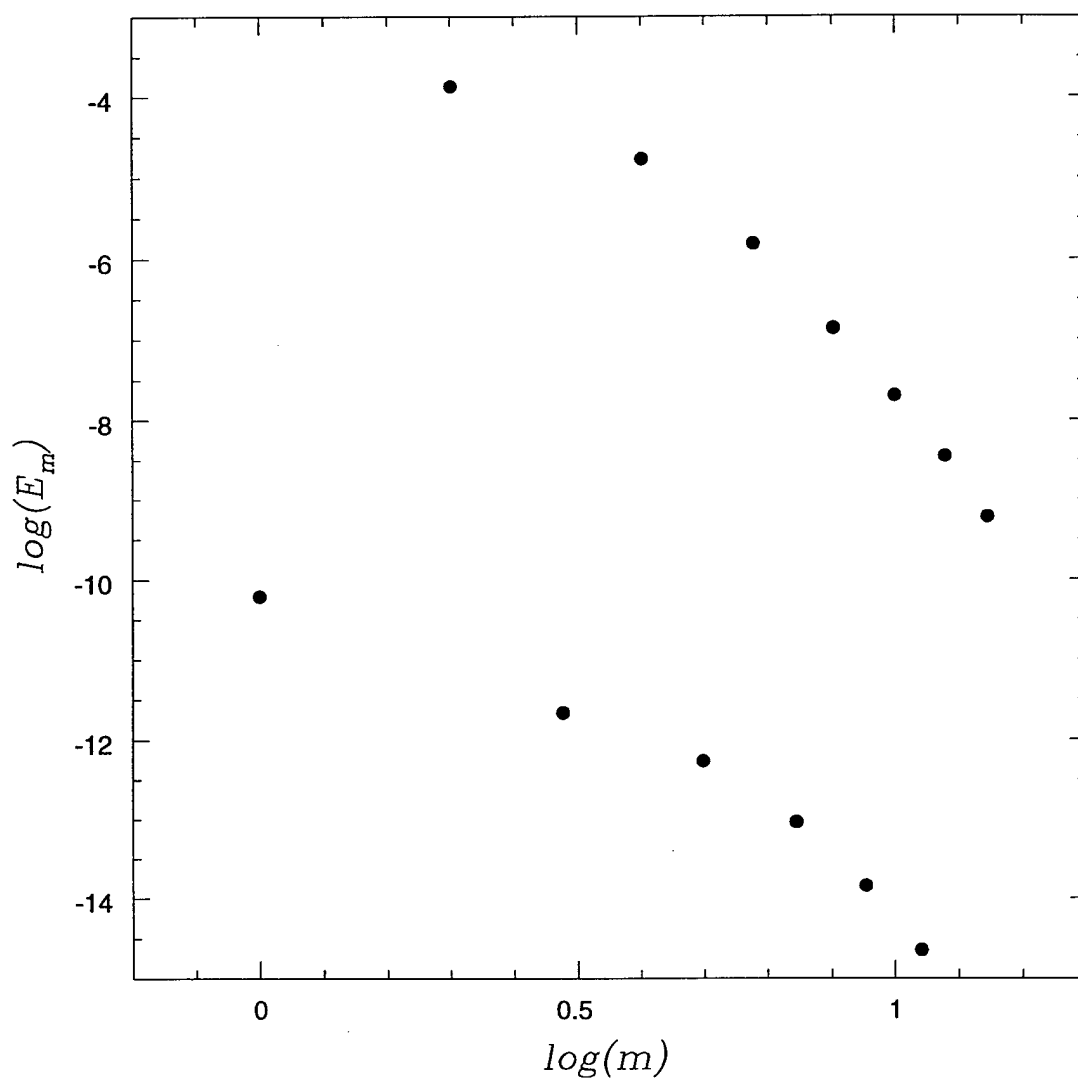
Figure 16: A typical azimuthal energy spectrum for the case with rotation and differential rotation
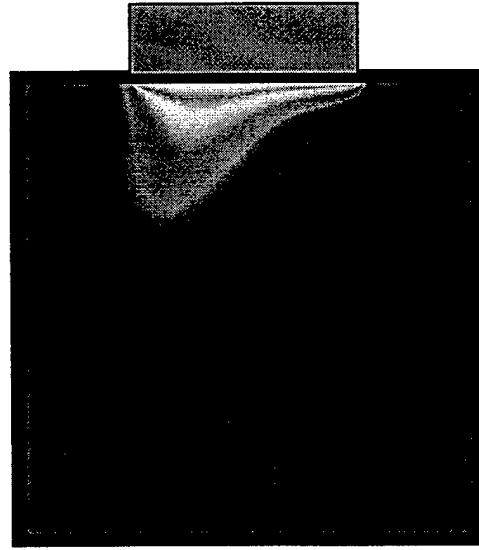
No Rotation
$Gr=2.8x10^6$

Axial U
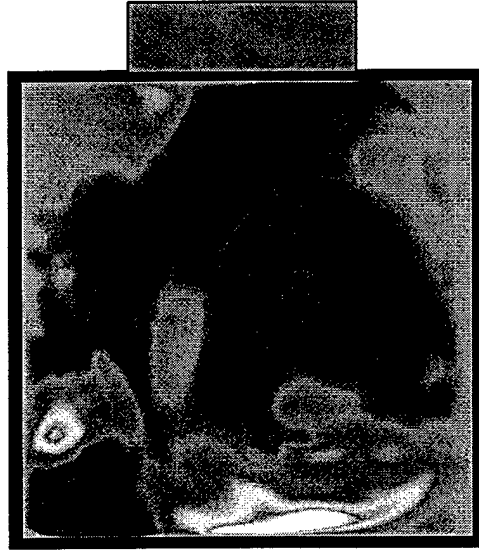
Radial V

Azimuthal W

Temperature T

Figure 17: Instantaneous isocontours of flow variables on a $r - z$ plane for case with only heating
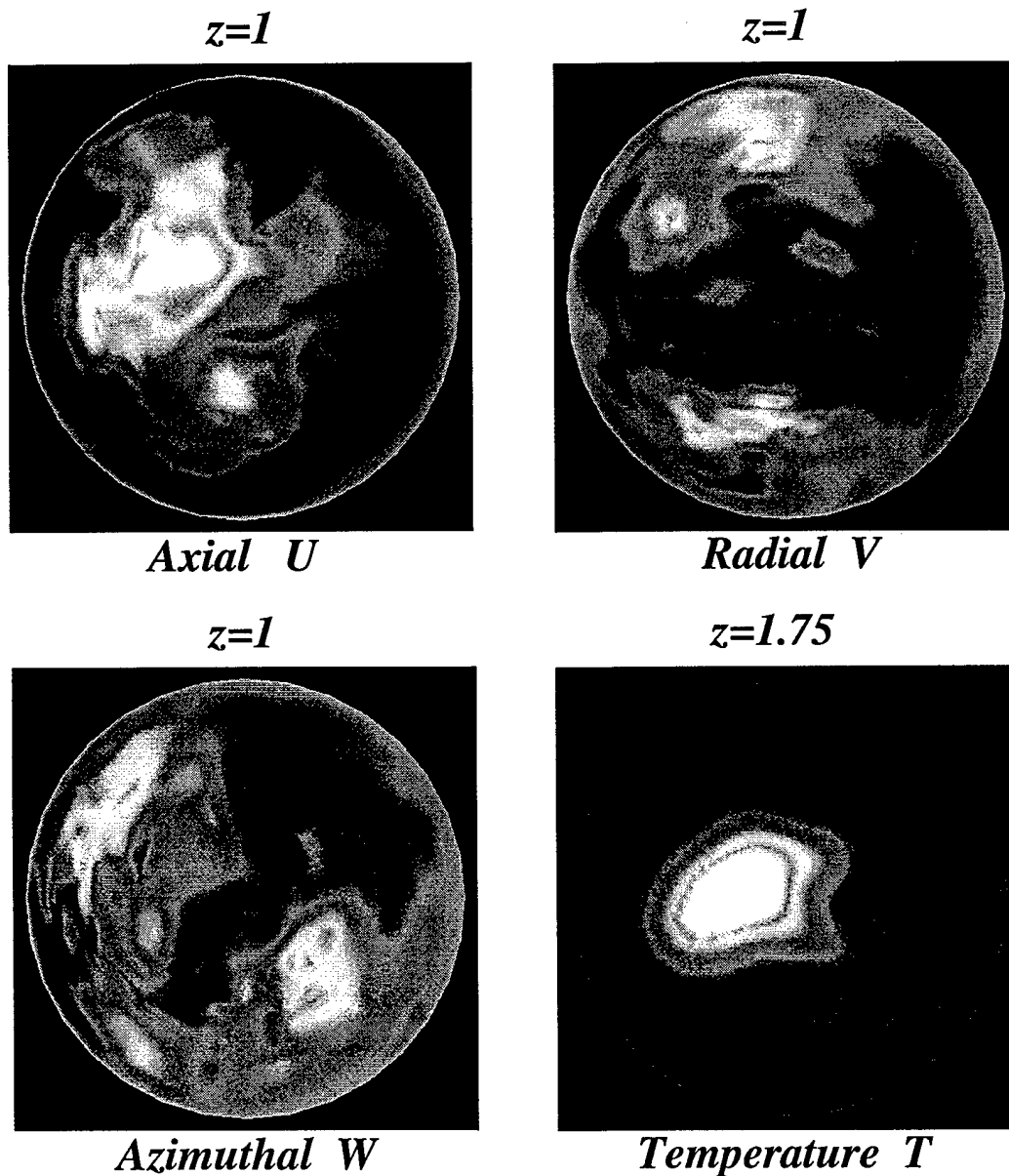
No Rotation

$Gr=2.8x10^6$

Figure 18: Instantaneous isocontours of flow variables on a $r - \phi$ plane for case with only heating

evidence of any symmetries present in the flow.

3.2.2 Low aspect ratio crucible H/D=0.25

The 3-D runs were performed using the axisymmetric steady state result as initial condition, with a 10^{-6} perturbation in the $m = 1$ azimuthal mode. As figure (21) shows, the even modes ($m = 2, 4...$) increase exponentially in amplitude, whereas the odd modes don't start to pick up until after the even modes have saturated to a certain amplitude. Rotation at an angular velocity $\Omega_1 = 1$ is turned on at $t = 247.5$. The flow becomes three dimensional for both cases (with or without rotation), however, the odd modes grow faster for the case without rotation and all modes saturate at slightly lower amplitudes when rotation is turned on. A typical instantaneous flow field, shown in terms of velocity and temperature isocontours, is plotted in figures (22), and (23), for the case with both heating and rotation. It can be observed in these figures that there exists a dominance of even modes in the flow, and in particular of the $m = 4$ azimuthal mode.

3.2.3 Rounded low aspect ratio crucible H/D=0.25

Preliminary 3-D simulations, without rotation, indicate that the flow also becomes three-dimensional, starting with the even modes, but these simulations have to be continued further. It is interesting to note that since the flow in low aspect ratio rounded crucibles seems to be less unstable than high aspect ratio crucibles with corners, one might be able to perform full three-dimensional numerical simulations at parameters (Gr, E, Ro) which are close to realistic values used in practice; that is to say that, although the same flow without rotation or even without differential rotation might be too chaotic to resolve with a DNS, the flow with all the stabilizing mechanisms turned on could be not out of reach. This does not necessarily mean that the resulting flow is axisymmetric.

Rotation

$$Gr=2.8x10,^6 \ E=Gr^{-1/2}=6x10^{-4}$$

Axial U

Radial V

Azimuthal W

Temperature T

Figure 19: Instantaneous isocontours of flow variables on a $r - z$ plane for case with heating and rotation

Rotation

$$Gr=2.8 \times 10^6, \ E=Gr^{-1/2}=6 \times 10^{-4}$$

z=1   z=1

Axial U   Radial V

z=1   z=1.75

Azimuthal W   Temperature T
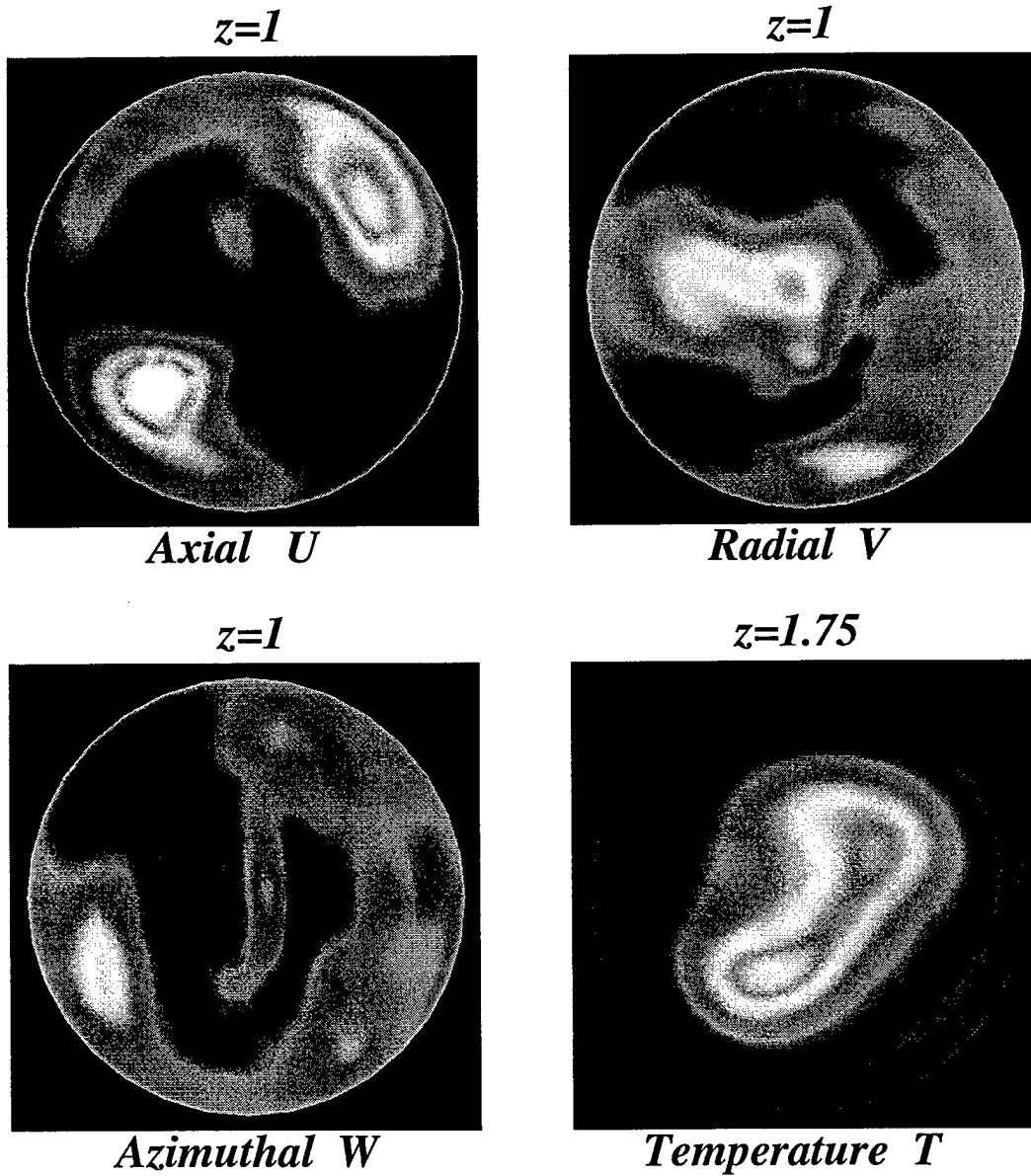
Figure 20: Instantaneous isocontours of flow variables on a $r - \phi$ plane for case with heating and rotation

31
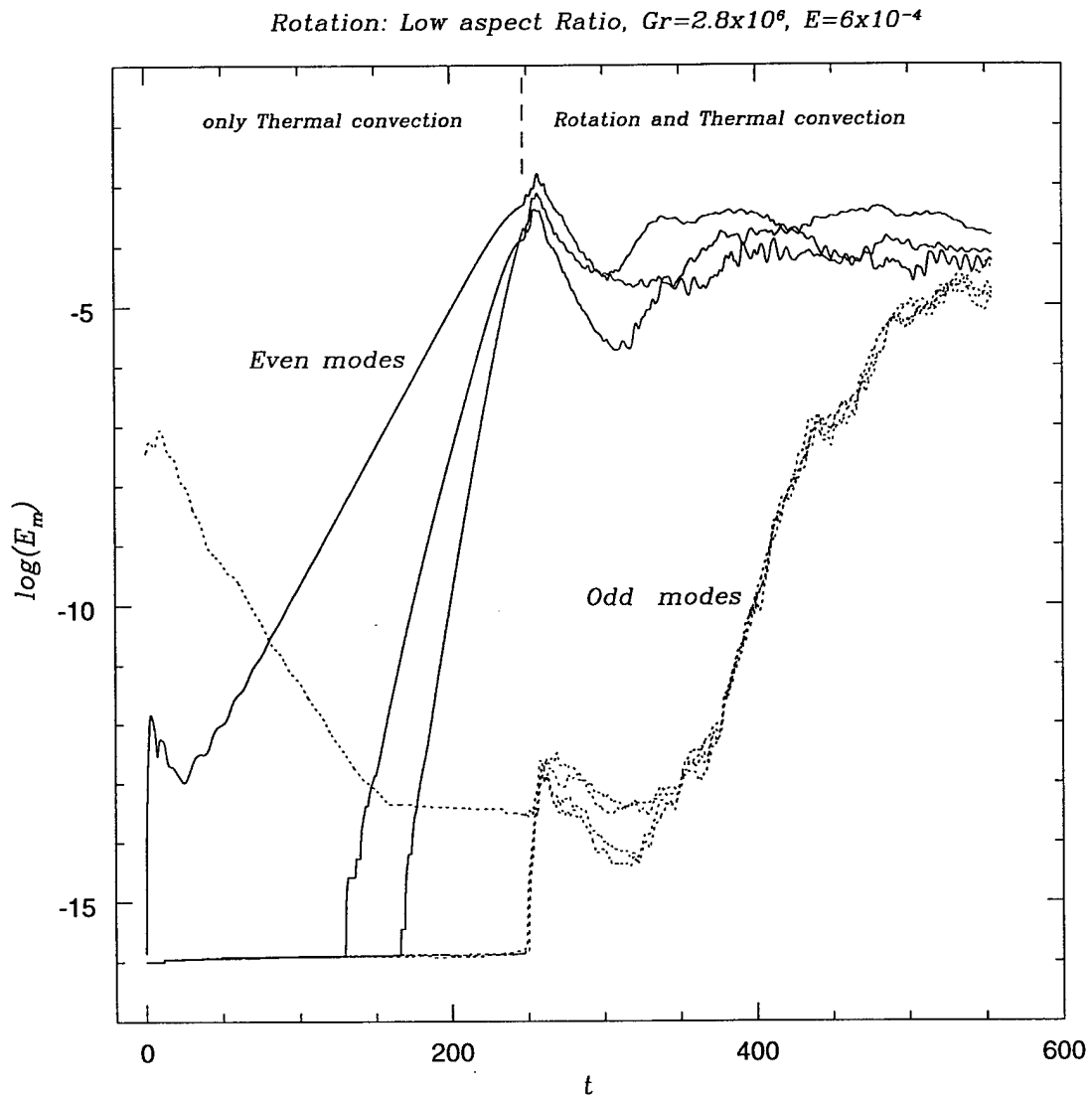
Figure 21: Time history of 3-D mode energies for flow in low aspect ratio crucible at $Gr = 2.8 \times 10^6$

Low aspect ratio crucible:
Rotation−thermal convection
$Gr=2.8x10^{6}, E=Gr^{-1/2}=6x10^{-4}$

z=0.5   z=0.5

Axial U   Radial V

z=0.5   z=0.875

Azimuthal W   Temperature T

Figure 22: Isocontours of axial velocity and temperature shown for a top view for the low aspect ratio crucible with heating and rotation.

Low aspect ratio crucible:

Rotation–thermal convection

$$Gr=2.8x10^{6}, E=Gr^{-1/2}=6x10^{-4}$$

Axial U

Radial V

Azimuthal W

Temperature T

Figure 23: Isocontours of axial velocity and temperature shown for a front view for the low aspect ratio crucible with heating and rotation.

3.3 Magnetic field simulations

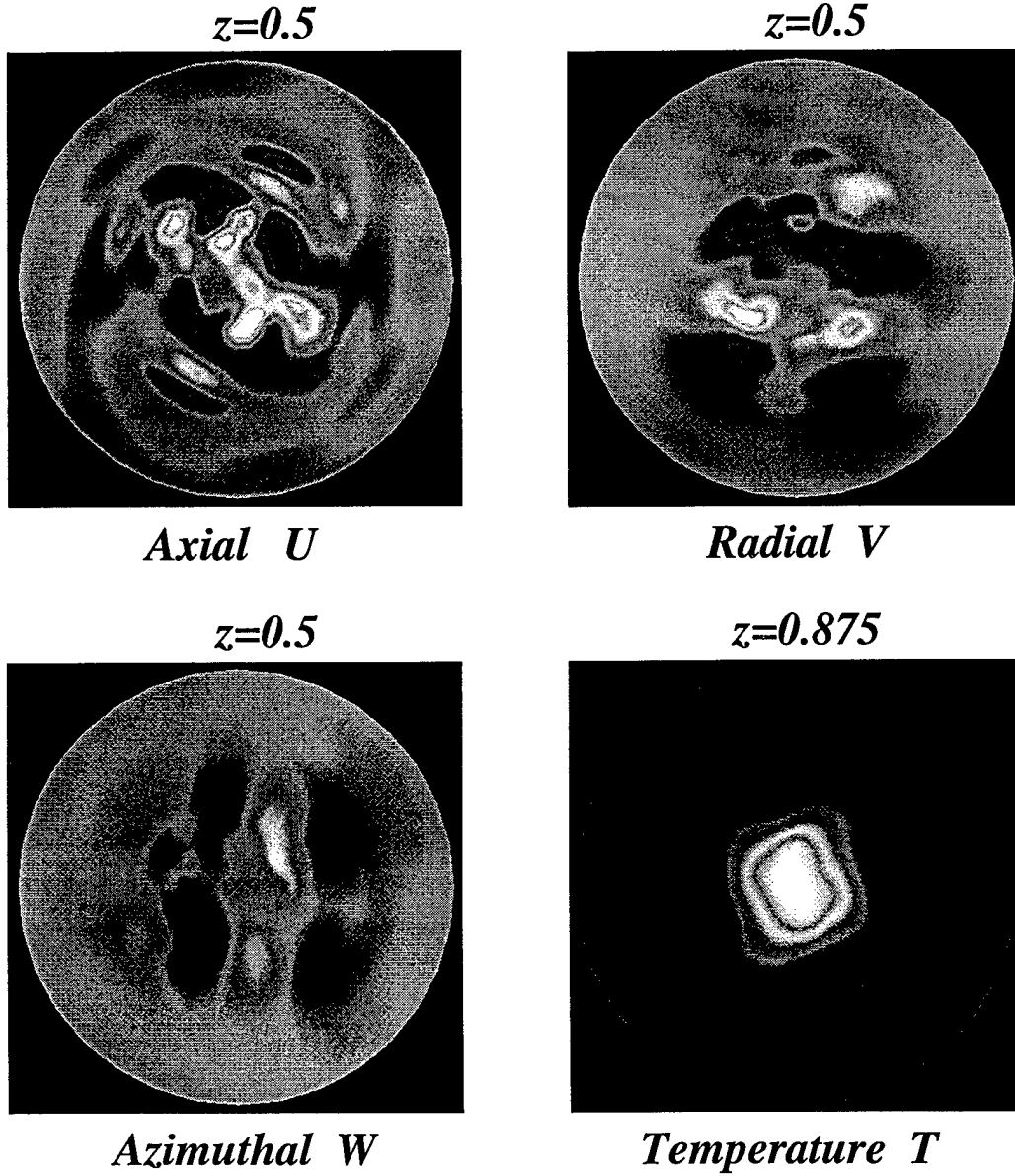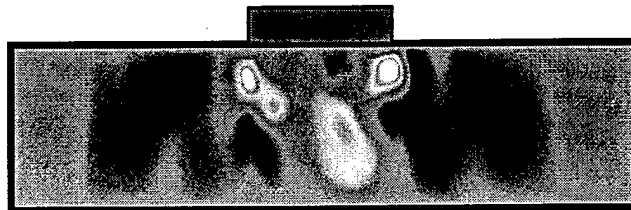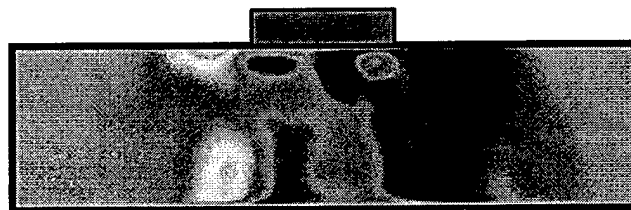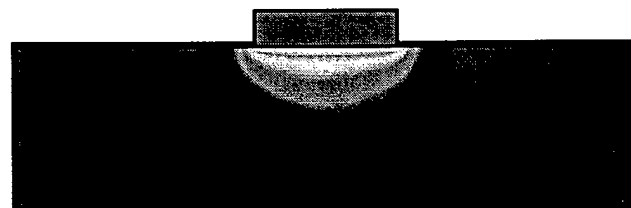Two different formulations have been developed and implemented for the case of an external magnetic field applied to the crystal melt. In the first one, we solve the full magnetic field and hydrodynamic equations, whereas in the other we assume that the magnetic Reynolds number Re_m is very small thereby allowing simplification of the solution procedure.

The governing MHD equations at the low magnetic Reynolds number limit are

$$\frac{\partial \mathbf{v}}{\partial t} + \mathbf{v} \cdot \nabla \mathbf{v} = -\nabla p - \frac{2\hat{k} \times \mathbf{v}}{Re\, E} + \frac{1}{Re}\nabla^2 \mathbf{v} + T + N\mathbf{j} \times \mathbf{B_0}$$

$$\mathbf{j} = -\nabla \phi + \mathbf{v} \times \mathbf{B_0}$$

$$\nabla^2 \phi = \nabla \cdot (\mathbf{v} \times \mathbf{B_0})$$

$$\frac{\partial \phi}{\partial n} = \mathbf{n} \cdot (\mathbf{v} \times \mathbf{B_0})$$

Here, Re is again defined as $Re = Gr^{1/2}$, $\mathbf{B_0}$ is the imposed axial magnetic field, and ϕ is the electric potential corresponding to the induced electric field. We present our results in terms of the magnetic parameter $N = \frac{B_0^2}{\rho U^2} Re_m$. N is related to the Hartmann number by

$$Ha^2 = N Re = \frac{B_0^2}{\rho U^2} Re_m Re$$

Various simulations have been performed with the main focus being to understand the influence of the magnetic field on the melt flow. All simulations performed up to now employ an axial magnetic field, since a transverse one would automatically destroy axisymmetry (although will not necessarily increase fluctuations). From our simulations, it seems that the imposed magnetic field, depending on its amplitude, can either dampen three dimensionality or enhance it. This can be observed in Figure (24), where one sees that a magnetic field with a magnetic parameter $N = 1$ dumps all non-axisymmetric modes, whereas a value of

20 increases the amplitude of non-axisymmetric modes. In fact, an intermediate value, e.g. $N = 5$, reduces the amplitude of the non-axisymmetric modes but not to zero. In order to visualize the effect of the magnetic field on the flow field, stream-wise vorticity isocontours at $z = 1$ are plotted in figures (25a), (25b), (25c) and (25d). As can be seen in these figures, the resulting vortex shape for $N = 1$ (Figure 25a) is a circle, corresponding to an axisymmetric flow; on the other hand, for $N = 5$ (Figure 25b), the vortex shape is only slightly distorted from axisymmetry, whereas for $N = 10$ (Figure 25c) and 20 (Figure 25d) the main central vortex is distorted from a circular shape to an ellipse with a higher aspect ratio than the case without magnetic field, shown in figure (14). In addition, the vortex structure rotates with respect to the rotating crucible.

We have also extended the analysis due originally to Chandrasekhar (Oxford University Press, 1961) to analyze the effects of magnetic fields on the stability of Bénard convection. This analysis which involves the solution of a $12th$ order boundary value problem, leads to interesting insights on the mechanisms by which magnetic fields can be destabilizing, as shown in the following section.

3.3.1 Influence of rotation and magnetic field on the stability of thermal convection

The growing crystall is usually rotated as it is pulled. The objective is to improve uniformity by providing a viscous shear layer that tends to isolate the growth interface from the turmoil deeper in the melt. The crucible is also rotated to smooth out thermal asymmetries that might arise from irregularities in the heating. Sometimes the crystal melt is stabilized by the use of a magnetic field. Crystal rotation and magnetic field individually may suppress curtain instabilities, but combined together they may lead to new instabilities.

As an example of new instabilities, which could potentially arise by the combined use of rotation and magnetic field, we consider, following Chandrasekhar (1961) [9], the case of Rayleigh-Bénard convection in the presence of rotation and magnetic field. The convection is characterized by the Rayleigh number Ra, Prandtl number Pr, Taylor T or Ekman E numbers, with the Taylor number being $T = 1/E^2$, and the Hartmann number Ha.
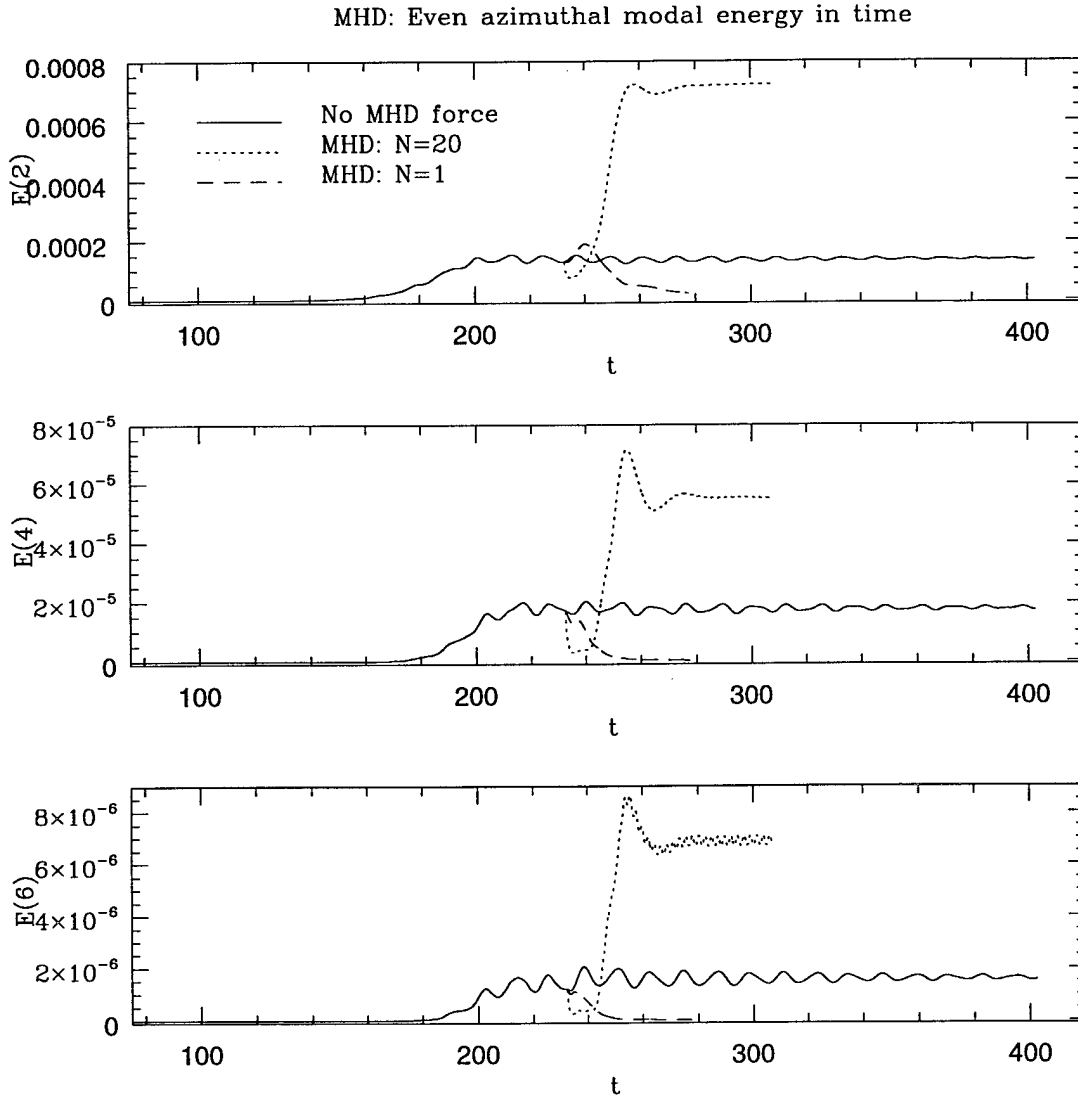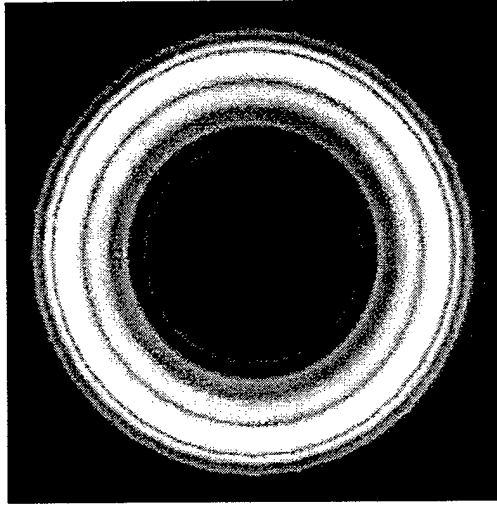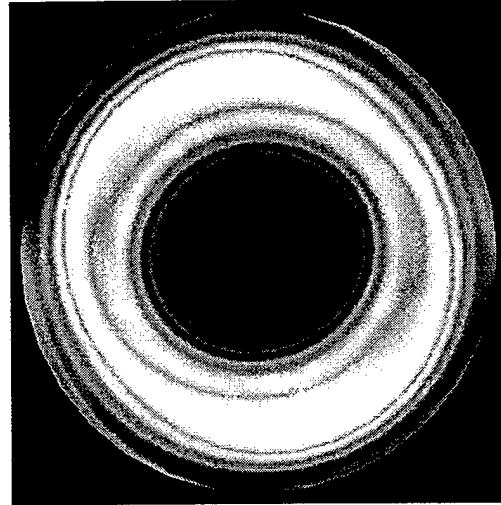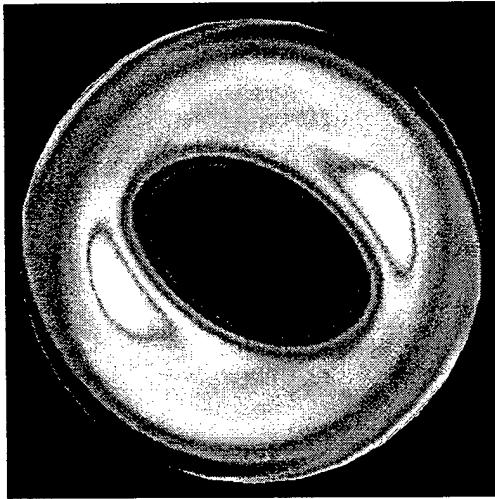
MHD: Even azimuthal modal energy in time

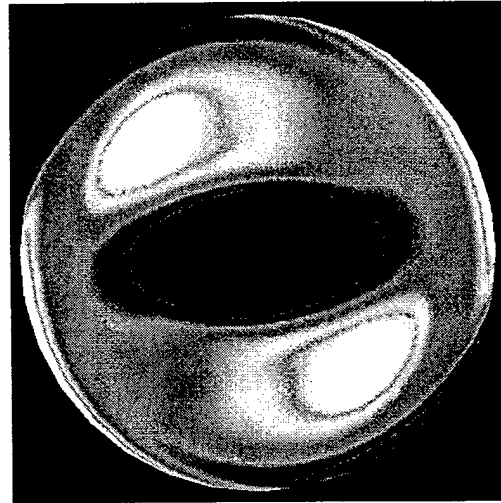Figure 24: Time history of the even azimuthal mode energy with the application of different magnetic fields

a) N=1

b) N=5

c) N=10

d) N=20

Figure 25: Isocontours of axial vorticity at $z = 1$ for the case with a magnetic field with a) $N = 1$, b) N=5, c) N=10, and d) N=20

Separately both rotation and magnetic field inhibit the onset of instability and they both elongate the cells which appear at marginal stability. These effects have a common origin: the flow becomes more two-dimensional. Acting together, however, they may lead to a new instability. The reason behind this is that rotation and magnetic field present together have conflicting interests. Rotation induces a component of vorticity in the direction of rotation. It results in the streamlines becoming closely wound spirals with motions principally confined to planes transverse to the rotation. On the other hand, a magnetic field would suppress the motion transverse to its direction and the motion along the magnetic field becomes dominant. In addition, the instability in the presence of rotation sets in as overstability, although it sets in as stationary convection when a magnetic field is present.

In the simplest case of two free boundaries the characteristic equation for the critical Rayleigh number takes the form

$$Ra = \pi^4 \frac{(1+x)\{[(1+x)^2 + Ha^2]^2 + T_1(1+x)\}}{x[(1+x)^2 + Ha^2]} \tag{8}$$

where

$$x = \frac{\ell^4}{\pi^4}; \quad \text{and} \quad T_1 = \frac{T}{\pi^4} \tag{9}$$

and ℓ is the characteristic scale of the onset of instability. These equations determine the instability threshold in the case of the onset of instability as stationary convection. In the case of the onset of instability as overstability the characteristic equations take the form

$$Ra = 2\pi^4 \frac{1+x}{x} \frac{(1+x)^2 + Ha^2}{(1+x)^2(1-Pr) - PrHa^2} \left[(1+x)^2 + Pr^2\sigma^2\right] \tag{10}$$

where

$$\sigma^2 = \frac{T_1}{1+x} \frac{(1+x)^2(1-Pr) - PrHa^2}{(1+x)^2(1+Pr) + PrHa^2} - \left[1 + x + \frac{Ha^2}{1+x}\right]^2 \tag{11}$$

These equations are accurate in the case of low magnetic Prandtl number which is always the case for crystal growth.

39

The solution of these equations for Ekman number equal to $E = 10^{-3}$ (or Taylor number 10^6) and Prandtl number $Pr = 0.2$ is shown in figure (26). Let us consider the stability of the flow with the increase of the magnetic field starting from Rayleigh numbers for which the flow is stable in the absence of the magnetic field. As can be observed the flow may become unstable at a certain level of the magnetic field. If we increase the strength of the magnetic field even further the flow stabilizes once again.

The effect of the destabilization of thermal convection by the action of a magnetic field in the presence of rotation is sensitive to the geometry, Prandtl number and configuration of temperature gradients. The stability of the flow in crystal melts in the presence of magnetic field and rotation should be studied using three-dimensional direct numerical simulation.

4 RNG-Based Modeling of Stratified Mixing

Renormalization group (RNG) methods are a general framework for "model building" in which the complex dynamics of physical problems is described in terms of so-called "coarse-grained" equations of motion governing the large-scale, long-time behavior of the physical system. The RNG approach allows coarse-graining of physical phenomena as varied as critical phenomena, high-energy physics, and, especially in the context of fluid dynamics, turbulence, combustion, and heat transfer. The key idea is that the RNG method is applicable to scale invariant phenomena lacking externally imposed characteristic length and time scales. For turbulence, this means that the method is applicable to the description of the small scales (small eddies) that should be statistically independent of the external conditions and dynamical forces that create them through various kinds of instability phenomena. In other words, the RNG method gives a theory of the so-called Kolmogorov equilibrium range of turbulence, especially comprising the so-called inertial range of small-scale eddies whose energy spectrum follows the famous Kolmogorov law $E(k) \sim k^{-5/3}$. The importance of the RNG results is, as we shall see, once the inertial range eddies can be accounted for in a qualitatively correct way, we may then obtain coarse-grained equations of motion for the other relevant variables of the turbulence, including, the mean velocity, rms velocities, etc.
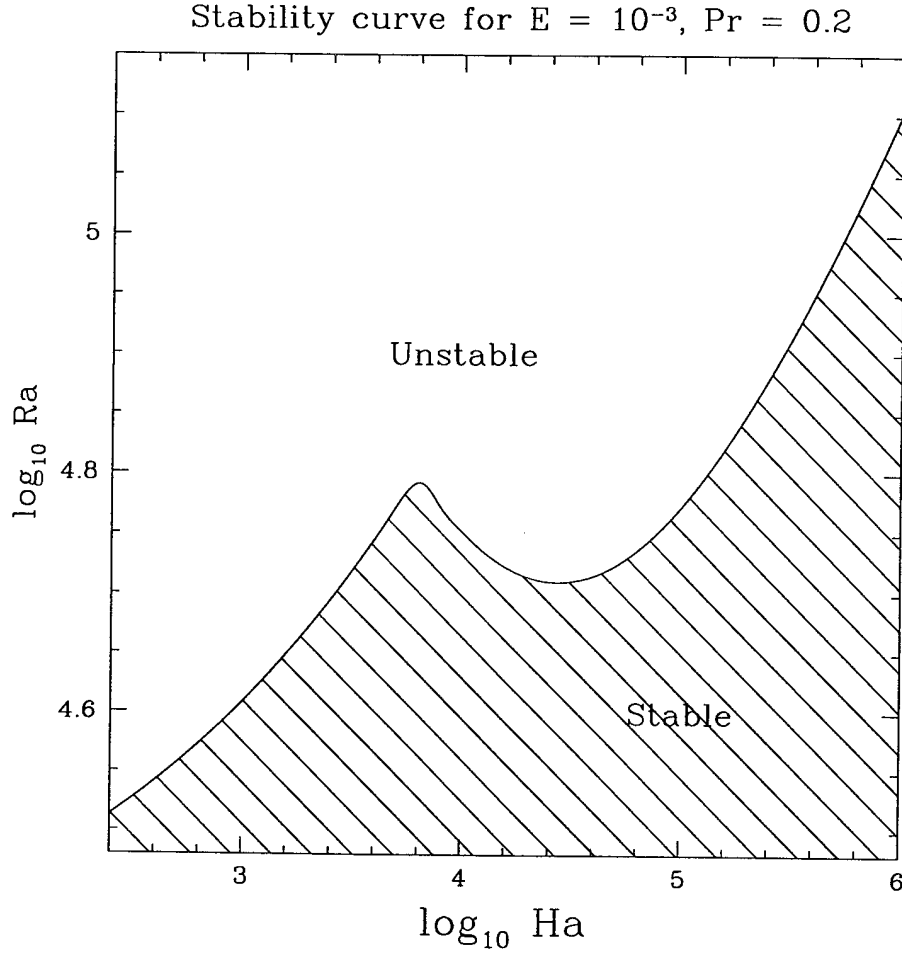
Figure 26: The stability diagram of critical Rayleigh number as the function of Hartmann number for Ekman number 10^{-3}

Summary of the RNG Method

In the application of RNG methods for turbulence modeling, the local turbulent kinetic energy K and the local energy dissipation rate $\mathcal{E}$ are used to eliminate the large-eddy length scale L from the dynamics, and the RANS equation of motion for U_i is supplemented by equations for K and $\mathcal{E}$. The RNG method is used to evaluate otherwise unknown terms in tehse equations for this $K - \mathcal{E}$ model.

The resulting RNG $K - \mathcal{E}$ model differs from classical (or standard) $K - \mathcal{E}$ models in at least six ways:

41

- At high Reynolds number, the constants in the RNG $K - \mathcal{E}$ model are evaluated by the theory;

- New terms appear like a rate of strain term, which is important for treatment of non-equilibrium effects and flows in the rapid distortion limit;

- Impulse response modifications, important for non-equilibrium effects, are also taken into account;

- Low Reynolds number modifications are given by the RNG theory, so wall function are no longer required;

- Modified boundary conditions are developed from the theory;

- Stratification and rotation (swirl) effects are accounted for by extensions of the RNG theory to stratified and rotating flow. Here we briefly describe these new effects as developed in the present work.

RNG modeling of stratified turbulence

We have initiated the derivation of turbulence transport models for vertical mixing based on the RNG analysis of stratified flows. This model will be used for the investigation of highly turbulent flow inside the stratified gas surrounding the crystal and the melt, or for very high Rayleigh numbers for the liquid flow inside the crucible as well. The classical theory of turbulent thermal convection is based on the following main ideas:

1. The physics of boundary layers is independent of the processes taking place in the bulk of the fluid outside the thermal boundary layers.

2. The energy and temperature spectra are $E(k) \sim E_T(k) \sim k^{-5/3}$. These assumptions are sufficient to derive the classical result that the Nusselt number Nu, a non-dimensional heat flux , satisfies

$$Nu \sim Ra^{1/3}$$

where Ra is the Rayleigh number. In recent years, these classical assumptions have been brought into question by Libchaber's experiments at Chicago which covered a broad range of Rayleigh numbers from 10^7 to more than 10^{14}. The surprising result of these carefully controlled experiments was that $E_T(k) \sim k^{-7/5}$ and $Nu \sim Ra^{2/7}$.

Recently, a theoretical explanation of these experiments has been given by V. Yakhot at CHI. The theoretical result shows that at intermediate Rayleigh numbers the Nusselt number scales as $Ra^{2/7}$, while at very large Rayleigh numbers $Nu \sim Ra^{5/19}$. At Rayleigh numbers of order of 10^{13}, the classical $Ra^{1/3}$ theory predicts heat fluxes that are an order of magnitude larger than those found by either the Libchaber experiments or the Yakhot theory.

An important outcome of the new theory is that the large-scale flow dynamics is governed by not the energy flux $\mathcal{E}$, but rather by entropy flux N at high Rayleigh numbers. Here, N is given by $N = \kappa \overline{(\nabla T)^2}$. Consequently, the effective viscosity is estimated as:

$$\nu_T = C'_\mu \frac{K \overline{T^2}}{N} \tag{12}$$

where K is the turbulence kinetic energy and C'_μ is a numerical constant. This formula replaces the $K - \mathcal{E}$ model

$$\nu_T = C_\mu \frac{K^2}{\epsilon},$$

for turbulent flows dominated by the energy flux. Therefore, in order to successfully model convective turbulence, equations for $K, \overline{T^2}$, and N are needed. The renormalization group analysis applied to this problem leads to a set of equations for $\frac{\partial K}{\partial t}$, $\frac{\partial \overline{T^2}}{\partial t}$, $\frac{\partial N}{\partial t}$, and $\frac{\partial \epsilon}{\partial t}$. These $K - \mathcal{E} - N$ turbulence transport equations have a form analogous to that of the RNG $K - \mathcal{E}$ equations which have already been successfully applied to complex turbulent flows with strong rotation, massive separation, flow transitions and other phenomena.

RNG description of anisotropic transport in stratified turbulence

The system of equations for mean velocity, U_i, mean temperature, T (relative to an 'ambient' temperature T_0), mean pressure P, mean turbulent kinetic energy, K and mean

energy dissipation rate, ϵ are

$$\frac{\partial U_i}{\partial t} + U_j\frac{\partial U_i}{\partial x_j} = -\frac{1}{\rho_0}\frac{\partial P}{\partial x_i} + \nabla_h(\nu_h\nabla_h U_i) + \frac{\partial}{\partial x_3}(\nu_z\frac{\partial U_i}{\partial x_3}) + g\beta\delta_{i3}T$$

$$\frac{\partial U_i}{\partial x_i} = 0$$

$$\frac{\partial T}{\partial t} + U_j\frac{\partial T}{\partial x_j} = \nabla_h(\kappa_h\nabla_h T) + \frac{\partial}{\partial x_3}(\kappa_z\frac{\partial T}{\partial x_3})$$

$$\frac{\partial K}{\partial t} + U_j\frac{\partial K}{\partial x_j} = \nabla_h(\frac{\nu_h}{\sigma_k}\nabla_h K) + \frac{\partial}{\partial x_3}(\frac{\nu_z}{\sigma_k}\frac{\partial K}{\partial x_3}) + \frac{\tau_{ij}}{\rho_0}\frac{\partial U_i}{\partial x_j} - g\beta\kappa_z\frac{\partial T}{\partial x_3} - \epsilon$$

$$\frac{\partial \epsilon}{\partial t} + U_j\frac{\partial \epsilon}{\partial x_j} = \nabla_h(\frac{\nu_h}{\sigma_\epsilon}\nabla_h \epsilon) + \frac{\partial}{\partial x_3}(\frac{\nu_z}{\sigma_\epsilon}\frac{\partial e}{\partial x_3}) + \frac{\epsilon}{K}(C_\tau\frac{\tau_{ij}}{\rho_0}\frac{\partial U_i}{\partial x_j} - C_\rho g\beta\kappa_z\frac{\partial T}{\partial x_3} - C_\epsilon\epsilon)$$

Let us introduce parameter of stratification (buoayancy frequency)

$$\Omega \equiv \sqrt{(g\beta|\frac{\partial T}{\partial x_3}|)}$$

Corresponding dimensionless parameter is

$$\zeta = \Omega K/\epsilon$$

Following Prandtl numbers can be defined as

$$\alpha_1 \equiv \nu_h/\nu_{iso},$$

$$\alpha_2 \equiv \nu_h/\nu_z,$$

$$\alpha_3 \equiv \nu_h/\kappa_h,$$

$$\alpha_4 \equiv \nu_h/\kappa_z$$

Here $\nu_{iso} = C_\mu\frac{K^2}{\epsilon}$. All Prandtl numbers are functions of ζ only.

The system of the RNG equations for these anisotropic Prandtl numbers has the following form:

$$\frac{d\alpha_i}{d\zeta} = f_i(\alpha_1,\alpha_2,\alpha_3,\alpha_4,\zeta). \quad i = 1,2,3,4$$

where the RNG theory determines the explicit form of the function f_i. It is these equations that provide for the effective treatment of stratified flows.

44

5 Future work

The work described here provides significant insights into the kinds of fluid dynamical effects important to the MLEK process. In particular, our results on flow stabilization by rotation, differential rotation and magnetic fields should have substantial impact on the choice of operational flow regimes for successful crystal growth by the MLEK process. However, much additional work needs to be done. In particular, additional work on the following kinds of problems is important for practical applications:

- Heat losses to the gas: Detailed consideration of modification of the flux boundary condition at the free surface must be given to account for typical radiative or convective heat losses to the surrounding gases.

- Interface tracking: An adaptive remeshing algorithm for interface tracking will have significant impact, since the interface shape between the melt and the crystal and between the melt and the gas has to dynamically be updated during the calculation. For this, a spectral element adaptive algorithm similar to the one for moving boundaries will, we believe, be most effective.

- Thermal stresses in crystal: Having calculated the shape and and temperature distribution along the interface, the temperature and stress distribution inside the crystal can be obtained. From the stress distribution, a density of dislocations can be obtained inside the crystal which can give information about the quality of the crystal produced.

- Multi-species composition: Another interesting direction is the incorporation of different species concentrations as part of the melt composition. This is now straightforward numerically, but its difficulty lies in the fact that initial and boundary conditions might not be available or traceable from experiments.

References

[1] S.A. Orszag, A.G. Tomboulides, V. Borue, W. Flannery, *AIAA*, paper No. 97-0431 (1997).

[2] A.D.W. Jones, "An experimental model of the flow in Czochralsi growth", *J. of Crystal Growth*, **61**, 235-244 (1983).

[3] M.R. Malik, S.P. Wilkinson and S.A. Orszag, "Instability and transition in rotating disk flow", *AIAA Journal*, **19**, 1131-1138 (1981).

[4] M.H. Rogers, G.N. Lange, "The rotationally symmetric flow of a viscous fluid in the presence of an infinite rotating disk", *J. Fluid Mech.* **7**, 617-631, (1960).

[5] M. Mihelcic, K. Wingerath, "Instability of the boyancy driven convection in Si melts during Czochralski crystal growth. ", *J. of Crystal Growth* **97**, 42-49, (1989).

[6] G.P. Williams, "Numerical integration of the three-dimensional Navier-Stokes equations for incompressible flow", *J. Fluid Mech.* **37**,727-750, (1969).

[7] G.P. Williams, "Baroclinic annulus waves", *J. Fluid Mech.* **49**,417-449, (1971).

[8] R. Hide and C.W. Titman, "Detached shear layers in a rotating fluid", *J. Fluid Mech.* **29**,39-60, (1967).

[9] S. Chandrasekhar, Hydrodynamic and hydromagnetic stability, Oxford, 1961.